Astron. Astrophys. 357, 697–715 (2000)

ASTRONOMY AND ASTROPHYSICS

A study of opacity in SOHO-SUMER and SOHO-CDS spectral observations

I. Opacity deduction at the limb

D.H. Brooks[1], **G.A. Fischbacher**[1], **A. Fludra**[2], **R.A. Harrison**[2], **D.E. Innes**[3], **E. Landi**[4], **M. Landini**[4], **J. Lang**[2], **A.C. Lanzafame**[5], **S.D. Loch**[1], **R.W.P. McWhirter**[2], **and H.P. Summers**[1]

[1] University of Strathclyde, 107 Rottenrow, Glasgow G4 0NG, UK
[2] Rutherford Appleton Laboratory, Chilton, Didcot OX11 0QX, UK
[3] Max-Planck-Institute for Aeronomy, 37189 Katlenburg-Lindau, Germany
[4] University of Florence, Department of Astronomy and Space Science, 50125 Florence, Italy
[5] University of Catania, Institute of Astronomy, 95125 Catania, Italy

Received 2 February 1998 / Accepted 15 February 2000

Abstract. A study is presented of the optical thickness of spectral lines of carbon, nitrogen and oxygen ions in the quiet sun. The observations consist of cross limb scans by the SUMER and CDS spectrometers on the SOHO spacecraft. A maximum likelihood spectral line fitting code has been adapted to analyse the multiplet profiles and to provide an assessment of errors in the count rates, especially of close lying components. Branching multiplet component ratios are presented as a function of position across the limb and contrasted with theoretical ratios in the optically thin case. The emergent fluxes are analysed in an escape probability model to deduce the optical thicknesses in the various spectral lines. Different specifications of the escape probability are examined. These are used to compare the observations with a geometric model of the emitting layer thickness across the limb and the thinning of the emitting layer above the limb. Classification of the deviations of quiet sun spectral line intensities from the optically thin case is given to assist in the critical selection of lines for differential emission measure analysis. This is linked to a general purpose code for the calculation of the influence of the line radiation fields on the local excited state population structure of the selected ions so that the fluxes in any spectral lines can be predicted. The Atomic Data and Analysis Structure (ADAS) was used for the atomic calculations and data of the paper.

Key words: atomic data – atomic processes – Sun: atmosphere – Sun: UV radiation

1. Introduction

The effects of opacity in solar spectral lines have been studied on a number of occasions (Jordan 1967; Doschek et al. 1976; Doyle & McWhirter 1980). Jordan established the technique of using branching ratios of lines arising from a common upper level to extract information on opacities from spectral observations. Doyle & McWhirter subsequently developed this same technique to study opacity at the solar limb and their work included a simple model of predicted line ratios from the region on-disk up to the limb. Escape probability and escape factor expressions have been developed by many authors (eg. Holstein 1947; McWhirter 1965; Irons 1979). More recently Kastner & Kastner (1990), Kastner & Bhatia (1989) and Kastner & Bhatia (1992) have developed extensively escape probability expressions and have used them for examining emergent intensities and optically thick population structures, both from a predictive point of view.

The present paper seeks to use and develop the quantitative approach of Doyle & McWhirter in an analysis of spectral data from the SOHO spacecraft spectrometers CDS and SUMER. There are three objectives in this new analysis. Firstly, the range of multiplets available in this study enables us to present some systematics of the incidence of opacity along iso-electronic sequences and for different types of line transition. Secondly, we extend the Doyle & McWhirter analysis to the case of lines with optical thicknesses significantly greater than unity on the solar disk. The Doyle & McWhirter specification of the escape probability is imprecise in these circumstances and can be improved by layer averaging. Doyle & McWhirter used a geometric model of the emitting layer thickness variation at the limb to describe the line ratio observations. The present data quality allows also modelling of the line ratios from the thinning atmosphere above the limb for which we construct three alternative models. Thirdly, we seek to be able to judge the suitability of lines observed by CDS and SUMER intended for use in differential emission measure analysis. Such analysis is subject to criticism on grounds of uncertainties of theoretical atomic physics, static stratified atmosphere assumptions and line selection and calibration. The present study allows the prediction of those lines which should be rejected (or intensity adjusted) because they are not optically thin.

Send offprint requests to: H.P. Summers

We take a special interest in assessing how atmospheric substructure affects our opacity analysis and so consider the effects of local brightenings on-disk, wavelength shifts on crossing the limb, spicule like structures off-limb and the effects of instrumentally scattered light.

2. SUMER observations

The SUMER instrument (Wilhelm et al. 1995) uses an off-axis parabolic mirror to focus radiation on the interchangeable entrance slit of a spectrometer. In the spectrometer a parabolic mirror is used to collimate the light from the entrance slit. The collimated beam is then directed to a plane scan mirror which deflects it on to a spherical concave grating whose movement is coupled to the scan mirror in such a way as to ensure the maintenance of the sharp focus of the image. Rotating the scan mirror changes the angle of incidence of the light on to the diffraction grating and hence the wavelength range of the dispersed radiation. Two alternative two-dimensional detectors are positioned in the focal plane of the grating to collect stigmatic images of the entrance slit. Microchannel plates with crossed delay lines are used for the detectors. Along the dispersion axis, the central 511 of the 1024 pixels are coated with KBr with the remaining pixels bare (there are also Lα attenuators at the detector edge) to allow optimisation of effi ciencies and the 27.0 mm detector length allows sampling of the spectrum in approximately 40 Å segments. The effective wavelength coverage of the detector A used for these observations was from 788 Å to 1610 Å in first order and from $\sim$500 Å to 805 Å in second order. The lower limit of 500 Å is essentially determined by the sensitivity imposed by the normal incidence reflections in the instrument.

2.1. The OPAC observing sequences

The observations were carried out on 1996 September 7 using the observing sequences OPAC-1, OPAC-2, OPAC-3 and OPAC-4. In these sequences the 120 arc sec entrance slit was placed on the east limb with the slit length oriented north - south on the Sun. The spatial raster was east-west and composed of 18 exposures of 100 s duration with 1.9 arc sec steps between them. After each exposure the full 44Å by 120 arc sec image was received. The central wavelengths of the spectral intervals and the slit widths were chosen so that the multiplets to be studied were optimally exposed.

Multiplets with high count rates were observed through the narrow, 0.3 arc sec slit in the sequence OPAC-1. The key multiplets measured in this sequence were O III $2s^2\ 2p^2\ ^3P$ - $2s\ 2p^3\ ^3D$ (832.7 Å), N III $2s^2\ 2p\ ^2P$ - $2s\ 2p^2\ ^2D$ (991.6 Å), Ne VI $2s^2\ 2p\ ^2P$ - $2s\ 2p^2\ ^4P$ (992.6 Å), C II $2s^2\ 2p\ ^2P$ - $2s\ 2p^2\ ^2S$ (1036 Å), N II $2s^2\ 2p^2\ ^3P$ - $2s\ 2p^3\ ^3D$ (1085.7 Å), C III $2s2p\ ^3P$ - $2p^2\ ^3P$ (1175 Å) and Si III $3s3p\ ^3P$ - $3p^2\ ^3P$ (1298.0 Å).

The sequence OPAC-2 covered weaker multiplets with wavelengths shortward of 1350 Å. The multiplets measured in this sequence were C II $2s^2\ 2p\ ^2P$ - $2s\ 2p^2\ ^2P$ (904.48 Å), C II $2s\ 2p^2\ ^4P$ - $2p^3\ ^4S$ (1010 Å), Si IV $2p^6\ 3p\ ^2P$ - $2p^6\ 3d\ ^2D$ (1128 Å), C II $2s^2\ 2p\ ^2P$ - $2s\ 2p^2\ ^2D$ (1335 Å) and N III $2s^2 2p\ ^2P$ - $2s2p^2\ ^2P$ (684 Å, 2nd order).

The OPAC-3 and OPAC-4 sequences covered multiplets longward of 1350 Å. These multiplets were observed both on the bare and the KBr parts of the detector because beyond 1350 Å the sensitivity of the bare drops off very rapidly. By placing the spectrum on the bare and the KBr it is possible to separate the first and second order line contributions (c.f. Curdt et al. 1997). The key multiplets measured in these sequences were O V $2s2p\ ^3P$ - $2p^2\ ^3P$ (760 Å, 2nd order), N III $2s^2 2p\ ^2P$ - $2s2p^2\ ^2S$ (763 Å, 2nd order), N III $2s2p^2\ ^4P$ - $2p^3\ ^4S$ (772 Å, 2nd order), O IV $2s^2 2p\ ^2P$ - $2s2p^2\ ^2D$ (787 Å, 2nd order) and the O IV $2s^2\ 2p\ ^2P$ - $2s2p^2\ ^4P$ (1397.2 Å, 2nd order), O III $2s^2 2p^2\ ^3P$ - $2s2p^3\ ^3P$ (703 Å, 2nd order) and S VI $2p^6\ 3p\ ^2P$ - $2p^6 3d\ ^2D$ (706.4 Å, 2nd order).

2.2. Spectral fitting

The spectral observations were fitted with Gaussian profiles by a procedure (ADAS602) described by Brooks et al. (1999).

2.3. Multiplet selection and spectral fitting

A limited set of multiplets have been chosen from the full OPAC data for detailed examination. The principal selection objectives were firstly to classify the spectral lines emitted by carbon, nitrogen and oxygen ions on the solar disk in quiet sun conditions according to how much they are affected by opacity and secondly in the same solar observation conditions, to establish the trend of optical thickness of like lines along isoelectronic sequences. The OPAC data sets allow examination in principle of several multiplets of the C II, C III, N II, N III, O III and O IV spectra. In practice, blending and overlapping of multiplet components greatly restrict the number of multiplets amenable to detailed study. A summary is given in Table 1 of the multiplets assessed. Four of these were then studied in detail.

2.3.1. C III $2s2p\ ^3P$ - $2p^2\ ^3P$ (1175 Å)

The spectral interval for this multiplet is shown in Fig. 1a. The key multiplet components for opacity studies and the intensity ratios conventionally used are 2-2 and 1-2 with ratio I(2-2)/I(1-2) (where the multiplet components are identified by the J quantum numbers of the relevant levels with the first J-value that of the lower level) and 0-1 and 2-1 with ratio I(0-1)/I(2-1). The principal difficulty is the overlap of the 1-1 and 2-2 components which requires care with handling by the spectral fitting program. A series of fittings were conducted exploring the imposition of constraints on widths and centroid position to seek improvement of the fit reliability. Improvement was assessed by the reduction in the uncertainties on the counts estimated by the fitting program. The optimal fit was achieved by allowing the centroid positions of lines 2-1, 1-0, 0-1 and 1-2 to float as the program's ability to located them is reliable, but to constrain the

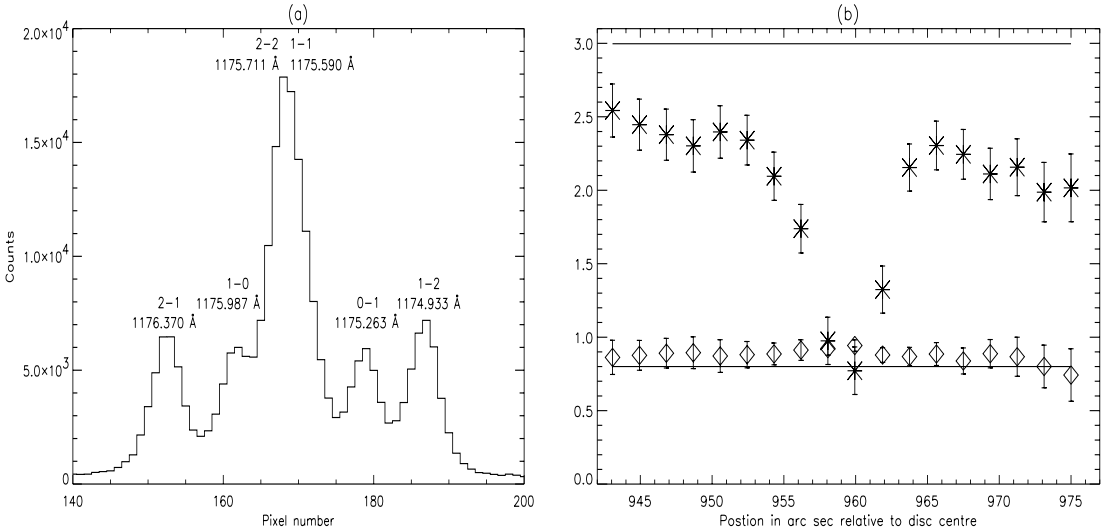

Fig. 1. **a** Spectral interval spanning the C III $2s2p\ ^3P$ - $2p^2\ ^3P$ (1175 Å) multiplet with component identification. The ordinate scale records the number of counts integrated along the line of sight and for each pixel along the wavelength scale measured in the 100 sec. of exposure time. **b** Branching line intensity ratios vs raster position in arc sec relative to the disc centre. The upper set of values corresponds to the I(2-2)/I(1-2) ratio and the lower set to the I(0-1)/I(2-1) ratio. The solid lines show the corresponding A-value ratios.

Table 1. Summary of OPAC multiplet suitability for opacity analysis. *Not analysed since other C II multiplets show the range of opacity effects.

Central wavelength	Multiplet	Comments
818.69 Å	O III $2s^22p^2\ ^3P$ - $2s2p^3\ ^3D$ (833 Å)	some blending
1004.95 Å	N III $2s^22p\ ^2P$ - $2s2p^2\ ^2D$ (992 Å)	unmanageable blending
1050.65 Å	C II $2s^22p\ ^2P$ - $2s2p^2\ ^2S$ (1036 Å)	suitable for analysis
1069.45 Å	N II $2s^22p^2\ ^3P$ - $2s^22p^2\ ^3D$ (1086 Å)	unmanageable blending
1160.65 Å	C III $2s2p\ ^3P$ - $2p^2\ ^3P$ (1175 Å)	suitable for analysis
918.27 Å	C II $2s^22p\ ^2P$ - $2s2p^2\ ^2P$ (904 Å)	suitable for analysis
1350.00 Å	C II $2s^22p\ ^2P$ - $2s2p^2\ ^2D$ (1335 Å)	suitable for analysis *
1370.17 Å	N III $2s^22p\ ^2P$ - $2s2p^2\ ^2P$ (684 Å)	suitable for analysis
1535.85 Å	N III $2s^22p\ ^2P$ - $2s2p^2\ ^2S$ (763 Å)	1/2-1/2 component badly blended with Si II $3p\ ^2P_{1/2}$ - $4s\ ^2S_{1/2}$

positions of the other lines relative to lines 2-2 and 1-1, allowing them to track their shift at the limb (see Sect. 2.5 and Fig. 7b).

The intensity ratios I(2-2)/I(1-2) and I(0-1)/I(2-1) are plotted against magnitude of the distance from sun centre in Fig. 1b. The latter ratio remains close to its A-value ratio indicating insensitivity to opacity at all raster positions across the limb. The individual lines of the latter ratio are in fact thin on disk and thicker at the limb but with very similar opacities. The former ratio approaches the optically thin value towards the disk, but deviates significantly on traversing the limb as the geometrical path length along the line of sight through the emitting layer lengthens. At raster positions above the limb, the ratio appears to return to the on-disk ratio rather than the optically thin ratio and is probably evidence of scattered light within the instrument. This movement in the ratio occurs at the same raster positions as the wavelength limb shift (see Sect. 2.5). Evidently the 2-2 line is nearly optically thin on disk but becomes thicker at the limb.

2.3.2. C II $2s^22p\ ^2P$ - $2s2p^2\ ^2S$ (1036 Å)

For this multiplet the components for opacity studies are 1/2-1/2 and 3/2-1/2 with the intensity ratio I(3/2-1/2)/I(1/2-1/2). There is no overlapping line problem in this case. However, there is a strong O VI line to the red of the 3/2-1/2 component which caused some difficulties in fitting the weaker C II features. As well as the O VI line there are two very small unidentified lines on either side of the C II multiplet. The spectral interval is shown in Fig. 2a. The two weak features became significant after the twelfth raster position, that is on crossing to above the limb. A consequence of this was that the autolooping option on the ADAS602 fitting procedure could not be used for the whole raster scan. The looping was then split into three sets of twelve, six and one raster position with five, three and three fitted features respectively. There was a small amount of line bending, so a line straightening program was run on all the raster positions. Various fitting options were performed in order

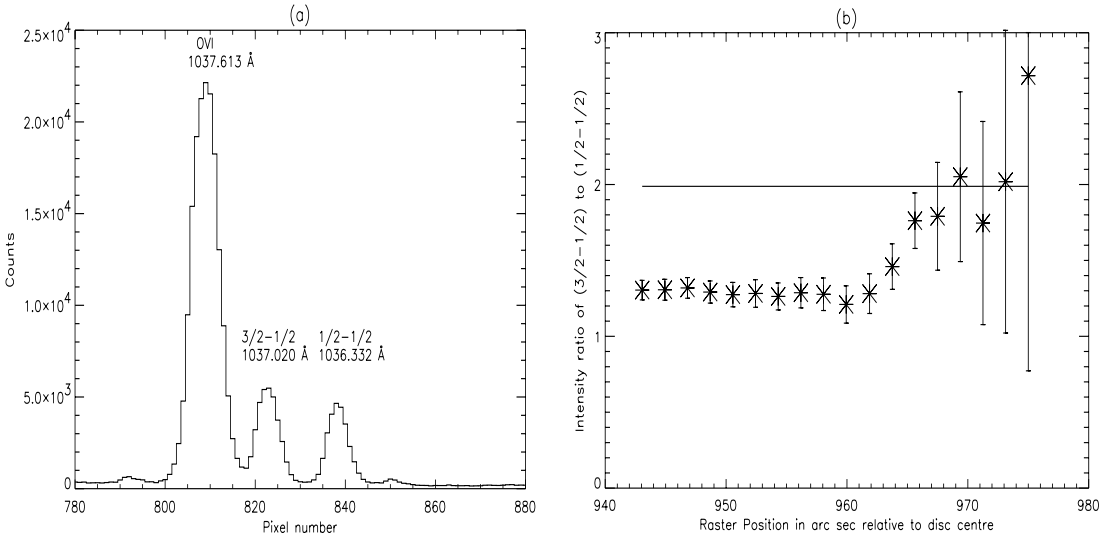

Fig. 2. **a** Spectral interval spanning the C II $2s^2 2p\ ^2P$ - $2s2p^2\ ^2S$ (1036 Å) multiplet with component identification. Ordinate scale as for Fig. 1a. **b** Branching line intensity ratios vs raster position in arc sec relative to the disc centre. The set of values corresponds to the I(3/2-1/2)/I(1/2-1/2) ratio. The solid line shows the corresponding A-value ratio.

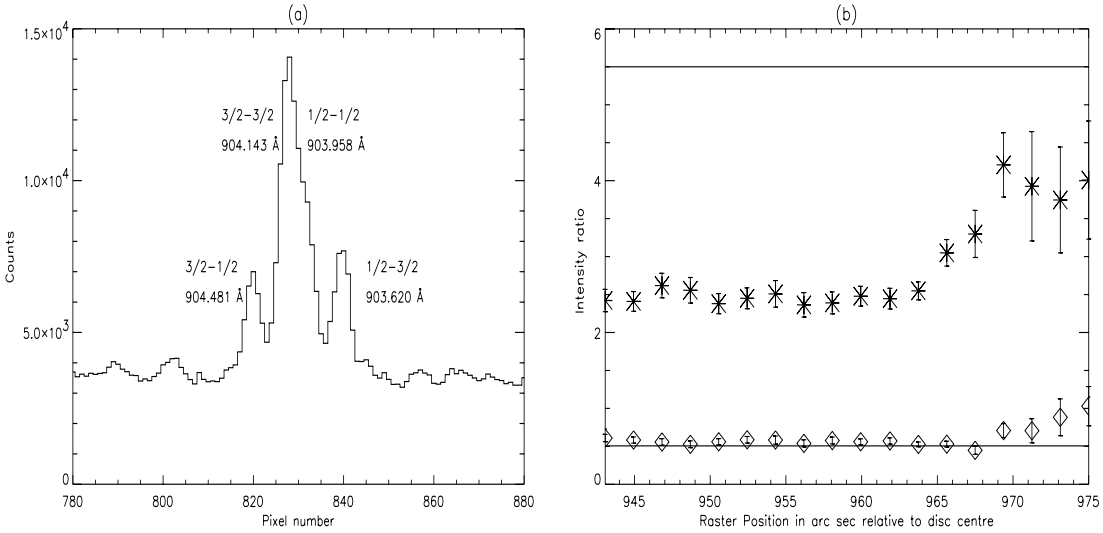

Fig. 3. **a** Spectral interval spanning the C II $2s^2 2p\ ^2P$ - $2s2p^2\ ^2P$ (904.48 Å) multiplet with component identification. Ordinate scale as for Fig. 1a. **b** Branching line intensity ratios vs raster position. The upper set of values with error bars corresponds to the I(3/2-3/2)/I(1/2-3/2) ratio and the lower set of values to the I(1/2-1/2)/I(3/2-1/2) ratio. The solid lines show the corresponding A-value ratios.

to achieve a fit with the minimum uncertainties in the estimate of the counts for the C II and O VI lines.

The I(3/2-1/2)/I(1/2-1/2) intensity ratio is shown in Fig. 2b and shows substantial deviation from the theoretical optically thin limit on disk. The ratio is relatively constant on crossing the limb and then moves towards the optically thin ratio above the limb. Both lines do not show much limb brightening confirming that they are optically thick on disk. This contrasts with the C III case since the more substantial self absorption orthogonal to the layer here affects local emitting ion population structure. The evidence for scattered light above the limb in Fig. 2b is less clear. The error bars are large due to O VI intensity dominating the weakening C II intensities in this region.

2.3.3. C II $2s^2 2p\ ^2P$ - $2s2p^2\ ^2P$ (904.48 Å)

The key multiplet components used for opacity studies are 3/2-1/2 and 1/2-1/2 with intensity ratio I(3/2-1/2)/I(1/2-1/2) and 3/2-3/2 and 1/2-3/2 with intensity ratio I(3/2-3/2)/I(1/2-3/2). The background intensity level is much higher for this multiplet than for the previous two and the 3/2-3/2 and 1/2-1/2 lines are strongly overlapping. However, the fitting procedure was able to resolve the components without difficulty. There are other adjacent line features, two to the red and three to the blue. Of these, one on each side blends into the C II multiplet. These features do not become significant until the fifteenth raster position just beyond the limb. The spectral interval is shown in Fig. 3a where the relatively high background is due to the Lyman continuum

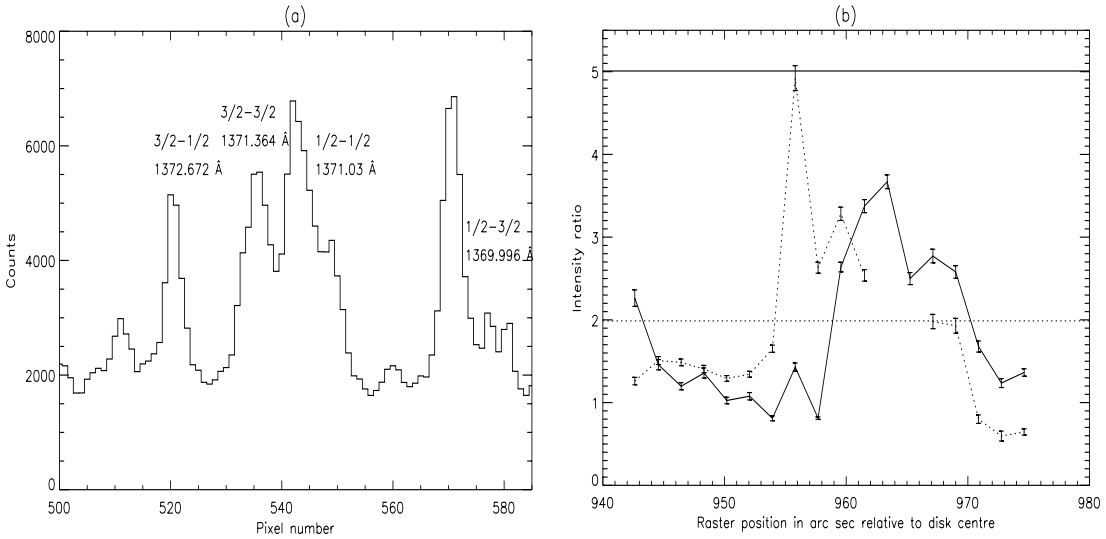

Fig. 4. **a** Spectral interval spanning the N III $2s^2 2p\ ^2P$ - $2s2p^2\ ^2P$ (684Å, 2nd order) multiplet with component identification. Ordinate scale as for Fig. 1a. **b** Branching line intensity ratios vs raster position. The solid line with error bars is the ratio I(3/2-3/2)/I(1/2-3/2) and the other solid line is the corresponding A-value ratio. The dotted line with error bars is the ratio I(1/2-1/2)/I(3/2-/1/2) and the other dotted line is the corresponding A-value ratio.

of hydrogen. There was a limb wavelength centroid shift (see Sect. 2.3.3) for the C II lines but its onset was higher above the limb than in the C III case. As before, error bars arise from the composite fitting error of the two component lines. The intensity ratio plots are shown in Fig. 3b. The solid lines show the corresponding A-value ratios. The graphs in this case contrast optically thick on disk and optically thin at limb ratios and are similar to ratios already illustrated in Fig. 1b and Fig. 2b. The ratio again suggests that scattered light is a major component of the off-limb observations with an onset in raster position close to that of the wavelength limb shift. The ratio's return to the on-disk values is not clear but it does show a marked deficit compared to the optically thin ratio well above the limb.

2.3.4. N III $2s^2 2p\ ^2P\ -\ 2s2p^2\ ^2P$ (684 Å, 2nd order)

The multiplet at 684 Å was observed in second order around 1368 Å. The spectral interval is shown in Fig. 4a. The key multiplet components used for opacity studies are 1/2-1/2 and 3/2-1/2 with the intensity ratio I(1/2-1/2)/I(3/2-1/2), and 3/2-3/2 and 1/2-3/2 with I(3/2-3/2)/I(1/2-3/2). Severe blending affects all but the 3/2-1/2 component. Attempts to separate the other components from their blended neighbours were largely unsuccessful in the first instance. However, a series of fittings were conducted to obtain the results. First, the 3/2-1/2 component was fitted separately in the interval 500 to 527 pixels in order to obtain estimates of its width. The width should be the same for each member of the multiplet. The interval 555 to 585 pixels was then fitted, fixing the widths of all lines to be the same as the 3/2-1/2 component. This allowed identification of the 1/2-3/2 component by its position (from a rough wavelength calibration using the values of Wilhelm et al. 1995) and its intensity relative to the 3/2-1/2 component. The positions of all lines were then fixed (along with the widths) and the fitting redone. Using the newly found pixel position of the 1/2-3/2 component, an improved wavelength calibration was calculated to obtain pixel positions for the 3/2-3/2 and 1/2-1/2 components. Poor separation of these components created a problem that was resolved by subtracting the background, estimated from the fit to the interval 555 to 585, from the intervals 500 to 527 and 526 to 556. Then the 3/2-1/2 component was fitted again with its position fixed and the updated values of its width used to fix the widths of all the lines within the 526 to 556 pixel interval. Comparison of the estimated positions and estimated intensities of the lines with their expected positions and expected intensities allowed their probable identification through the majority of the raster position datasets. However, when the lines were too weak off limb they could not be unambiguously separated and hence two unrealistic points are missing from Fig. 4b. The estimated positions were then used to fix the line positions and the fitting redone with the widths also fixed. This was our best attempt at the spectral fitting and produced the results shown in Fig. 4b. Due to the great attention paid to the fitting and its optimisation by analysis of estimated errors the error bars overplotted are very small. This reflects the success of the method described above in producing a 'good' fit. However, the appearance of up to 9 unidentified lines in the 526 to 556 interval reduces our confidence in whether the lines have truly been identified correctly. In the figure, the I(3/2-3/2)/I(1/2-3/2) ratio is the solid line with error bars and the straight solid line is the corresponding theoretical A-value ratio. The I(1/2-1/2)/I(3/2-1/2) ratio is the dotted line with error bars and the straight dotted line is its theoretical A-value ratio. Note the discontinuity for the reason described above. The error bars arise from the composite fitting error of the two component lines. The erratic results for the multiplet ratios preclude further deductive analysis in this case.

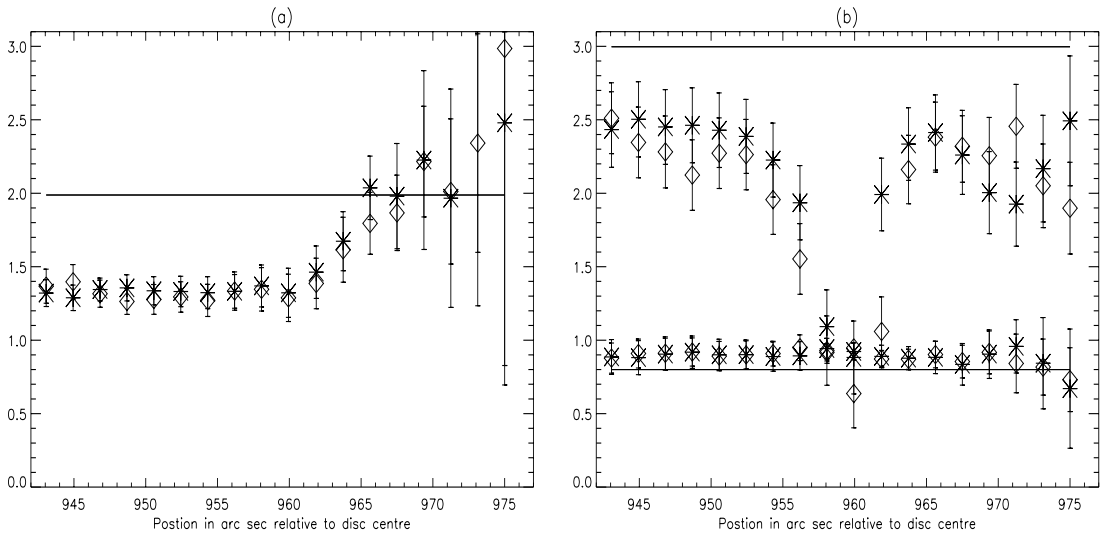

Fig. 5. **a** Branching line intensity ratios for the C II $2s^2 2p\ ^2P$ - $2s2p^2\ ^2S$ (1036 Å) multiplet vs raster position. The values with error bars correspond to the I(3/2-1/2)/I(1/2-1/2) ratio. The solid line shows the corresponding A-value ratio. Diamonds denote the brighter pixel group and diagonal crosses denote the weaker pixel group. **b** Branching line intensity ratios for the C III $2s2p\ ^3P$ - $2p^2\ ^3P$ (1175 Å) multiplet vs raster position in arc sec relative to the disc centre. The upper set of values corresponds to the I(2-2)/I(1-2) ratio and the lower set to the I(0-1)/I(2-1) ratio.

2.4. Variability along the slit

The analysis in this paper uses spectral data summed along the slit to deduce opacities. The OPAC observations spanned quiet sun regions, but there are significant random short term local brightness variations along the slit presumably due to the network. These are also on a short spatial scale so that such variations at adjacent raster positions are uncorrelated. We have sought to assess the implications of this variability for opacity deductions using branching ratios. In optically thin plasma, the pure branching ratios are independent of such variations. In the optically thick case, line emission is observed essentially from plasma layers up to unit optical depth from the observer. The contributing geometrical depth is then self adjusting through brightness variations, however caused, and so again the ratios would be expected to be insensitive. The sensitivity of the line ratios to brightness variability is when the optical depth of the emitting layer is of order unity. To investigate this, at each raster position the brightest 60 and weakest 60 pixels were separately summed and the line ratio variations for each as a function of raster position plotted separately. Results for the C II $2s^2 2p\ ^2P$ - $2s2p^2\ ^2S$ (1036 Å) and the C III $2s2p\ ^3P$ - $2p^2\ ^3P$ (1175 Å) spectral intervals are shown in Fig. 5. In Fig. 5a, on disc where the ratio is optically thick, the bright and weak pixel cases agree. On crossing the limb, there is a tendency for the bright pixel case to indicate greater optical depth but the error bars are large. In Fig. 5b, where the I(2-2)/I(1-2) ratio is nearly thin on disk, the brighter pixel group is more optically thick and this difference is enhanced on crossing the limb. The surface plots of Fig. 6 show that on disk there is a large variability in the observed fluxes for both C II and C III. Although the C II fluxes are clearly the more variable (c.f. the strong bright point on disk in Fig. 6a), there is less variation in opacity on disk for the C II data than for C III. Note that Fig. 6a refers to a different C II multiplet from Fig. 5a but the trend is the same for both.

It is to be noted also that, in the thinning atmosphere above the limb, there is a weak tendency for the bright pixel case to be apparently less optically thick. However, the above limb results do not return to the optically thin ratio and we interpret this as the actual above limb emission being dominated by scattered light from the disk. The brighter pixel case, having more intense lines, might be expected to be less dominated by scattered light. Overall the brightness ratio between the bright and weak pixel cohorts can be as much as a factor ~ 2. The present results show that the brightness variation is primarily due to density variation. In conclusion, deduced on-disk optical depths are modestly influenced by the size of the area integrated over but the broad interpretation of our results, when summing over the whole slit, remains valid for the opacity study.

2.5. Anomalous wavelength shifts

In the spectral fitting alluded to in Sect. 2.2, aside from the usual expected data corrections such as flat fielding, line bending and line tilting etc., for which there are established correction procedures, an anomaly was found in that there was an apparent wavelength shift of uncertain origin on crossing the limb.

Using the spectral fitting program with the C III $2s2p\ ^3P$ - $2p^2\ ^3P$ (1175 Å) multiplet, spectral positions (pixel number) of the components of the multiplet were plotted as a function of raster number (see Fig. 7a). There was clear evidence of a shift of 1-2 pixels systematically in each component as the limb was crossed. This substantially exceeds the solar rotation shift ($\sim$0.003 pixel). It creates a problem in automatic use of the spectral fitting program when it cycles on the basis of fixed positions for each component. The situation is a sensitive one with

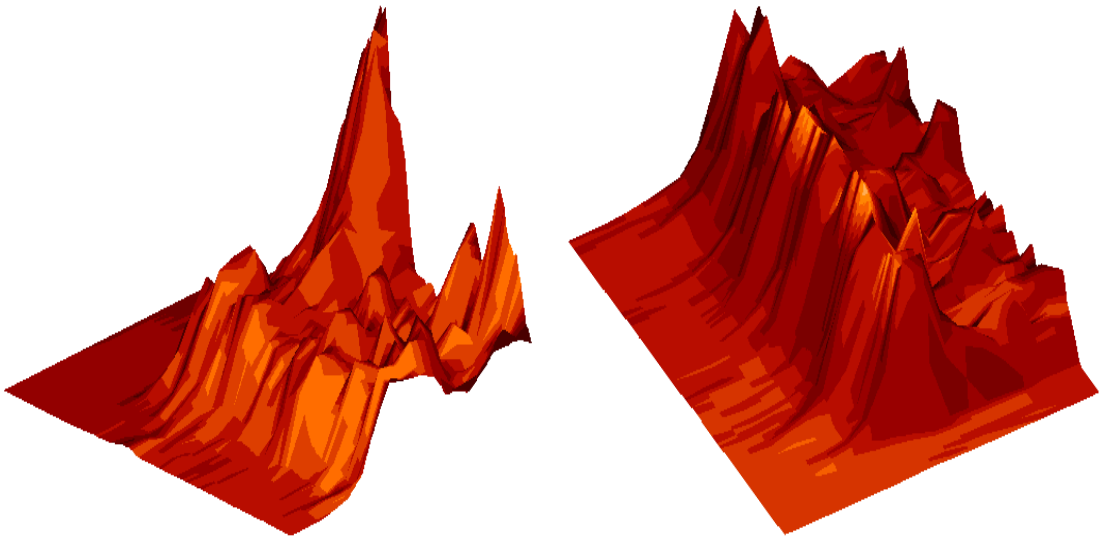

Fig. 6. **a** Surface plot of C II $2s^2 2p\ ^2P$ - $2s2p^2\ ^2P$ (904.48 Å) multiplet flux vs slit vs raster position. **b** As for **a** for C III $2s2p\ ^3P$ - $2p^2\ ^3P$ (1175 Å). In both cases the slit dimension runs from the bottom corner left and upwards while the raster dimension runs from the bottom corner right and upwards progressing from off-limb to on-disk. The flat regions to the left in **a** and to the right in **b** correspond to dead areas of the slit.

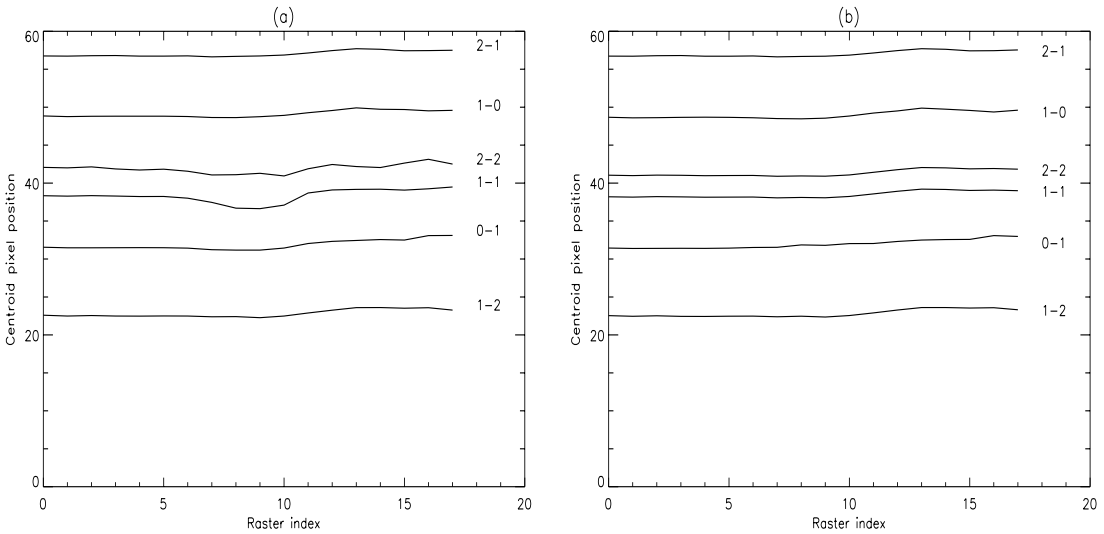

Fig. 7a and b. Pixel positions for the C III $2s2p\ ^3P$ - $2p^2\ ^3P$ (1175 Å) multiplet components as determined by the fitting code in automatic cycling mode. **a** The pixel positions of all the multiplet components are allowed to float. **b** A wavelength direction pixel shift vector determined from the well separated multiplet components, is imposed as function of raster position on the overlapped components. Components are labelled with the lower and upper j-values.

overlapped components, since fixed relative positioning is necessary for separation. Fig. 7a shows the systematic shift in the well resolved components (2-1, 1-2) and a spurious separation distortion from the fitting program at the limb ($\sim$ raster index 9) on the overlapped components (2-2, 1-1). We evaluated a pixel shift vector based on the average shift of the well separated 1-2 and 2-1 components at each raster point. This vector was then used with the looping fitting program for the overlapped components. The correction is shown convincingly in Fig. 7b. The limb shift varied in magnitude (up to $\sim$2.0 pixels) and onset in raster position between different multiplets. The origin of these shifts is unclear. Differential heating of the SUMER instrument with pointing is considered unlikely. We conjecture that they may arise from mass flows giving Doppler shifts in the observational line of sight. In the detailed line ratio studies of Sect. 2.3 it was pointed out that there are indications of scattered light dominating spectral intensities above the limb. It appears also that the onset of the wavelength shift coincides with the raster position at which scattered light dominates and not with the precise position of the limb. If so this implies that the scattered light (most probably a whole disk integral effect) has a blue shift relative to our limb observations of up to $\sim$ 20 km s^{-1}.

Fig. 8 shows the shift which was observed in the C II $2s^2 2p\ ^2P$ - $2s2p^2\ ^2P$ (904.48 Å) multiplet indicative of similar velocities as in the C III case.

No systematic shift was found in the fitted centroid positions for both the C II $2s^2 2p\ ^2P$ - $2s2p^2\ ^2S$ (1036 Å) and N III $2s^2 2p\ ^2P\ -\ 2s2p^2\ ^2P$ (684 Å) multiplets, neither is there clear evidence for scattered light in the ratios though in the latter case the ratios are, as stated in Sect. 2.3.4, erratic and we are uncertain as to their interpretation. In the C II case it is possible that the strong O VI line which dominated the fit to the C II 1036 Å multiplet components beyond the limb (see Sect. 2.3.2), masks both these effects if they are present.

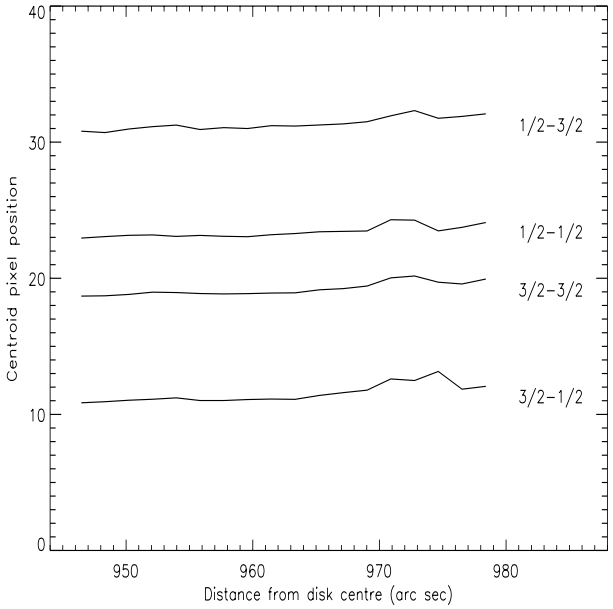

Fig. 8. Pixel positions for the C II $2s^2 2p\ ^2P$ - $2s2p^2\ ^2P$ (904.48 Å) multiplet components as determined by the fitting code in automatic cycling mode.

3. CDS observations

In the CDS instrument (Harrison et al. 1995) two portions of a Wolter-Schwartzschild type 2 telescope illuminate grazing and normal incidence spectrometers via a scan mirror and common entrance slit. The normal incidence instrument (NIS) is stigmatic, the incoming beam from the telescope being reflected from two toroidal diffraction gratings to an intensified CCD. The wavelength ranges are 308 - 381 Å (NIS1) and 513 - 633 Å (NIS2). To build up normal incidence images a line slit, in the present case 2 arc sec by 240 arc sec with its length orientated North - South on the Sun, was used and stepped across the solar image (from West to East) at the East limb using the scan mirror. The astigmatic grazing incidence spectrometer (GIS) was used with a 2 arc sec by 2 arc sec slit and scan mirror motion. The GIS is fitted with a concave reflection grating. The dispersed radiation is detected by four microchannel plate detectors placed around the Rowland circle covering the wavelength ranges 151 - 221 Å (GIS1), 256 - 338 Å (GIS2), 393 - 493 Å (GIS3) and 656 - 785 Å (GIS4). The GIS and NIS cannot be used simultaneously because of spacecraft power and telemetry limitations.

3.1. The NIS observing sequence

The NIS observing sequence ATRIC31 was run on 1997 March 13 and comprised five identical sequentially executed observations of the quiet Sun taken over an area of 3×1 arc min^2 area centered $\sim$ 20 arc sec above the East solar limb at the equator. Each observation was composed of 90 raster positions spaced 2.032 arc sec with a 70 s exposure time. The use of the narrowest available slit provided the best spatial and spectral resolution (useful for multiplet component resolution) possible for the NIS.

Each of the five different observations comprised full NIS1 and NIS2 spectra divided into 20 spectral windows, to minimize the effects of spectral slant. Recording the whole NIS spectrum instead of smaller portions restricted to the regions of the useful multiplets lengthened the total time by increasing the telemetry time without increasing the exposure time. Nevertheless, we felt it important to have the whole spectrum to give diagnostic information. In fact the increase in telemetry time was compensated for by only transmitting data from a 1 arc min length of the 4 arc min long slit. Density sensitive line intensity ratios indicated that the plasma observed in each of the five observations was not homogeneous. Large differences (sometimes more than a factor 2) in the emission of density insensitive lines were also observed. Some of the differences among the five observations are probably due both to solar rotation during the eleven hour run and to short timescale variations in line intensities.

3.2. Multiplet selection and spectral fitting

The most important multiplets to be studied with CDS are the $2s^2 2p\ ^2P$ - $2s2p^2\ ^2P$ quartets and $2s^2 2p\ ^2P$ - $2s2p^2\ ^2S$ doublets of the Boron-like ions from N III to Si X. As opacity effects are expected to affect only the lightest elements, only elements up to Neon have been considered in the present paper. A summary of the multiplets considered is given in Table 3.

Both the N III and Ne VI $2s^2 2p\ ^2P$ - $2s2p^2\ ^2P$ and $2s^2 2p\ ^2P$ - $2s2p^2\ ^2S$ transitions are in the GIS spectral range. The N III $2s^2 2p\ ^2P$ - $2s2p^2\ ^2P$ lines at 685 Å are weak, only three of the four expected lines are observed and are blended with a strong Si IX second order line as well as being in a region were it is likely that detector 'ghosts' coming from lines in the range 718 - 722 Å may be present. Detector 'ghosts' occur when strong lines in the spectrum cause spurious lines in other parts of the spectrum. This is due to one of the peculiarities of the GIS detector. The N III $2s^2 2p\ ^2P$ - $2s2p\ ^2\ ^2S$ doublet is very weak and recorded near a strong N IV line at 765 Å. The Ne VI $2s^2 2p\ ^2P$ - $2s2p^2\ ^2P$ lines around 400 Å are blended with second order lines from Mg VI and Fe XIII. It is also possible that 'ghosts' of the lines around 430 Å fall in that spectral range further confusing the situation. Similar problems are found for the weak Ne VI $2s^2 2p\ ^2P$ - $2s2p^2\ ^2S$ lines at 435 Å. Thus we discarded all the GIS lines from our study.

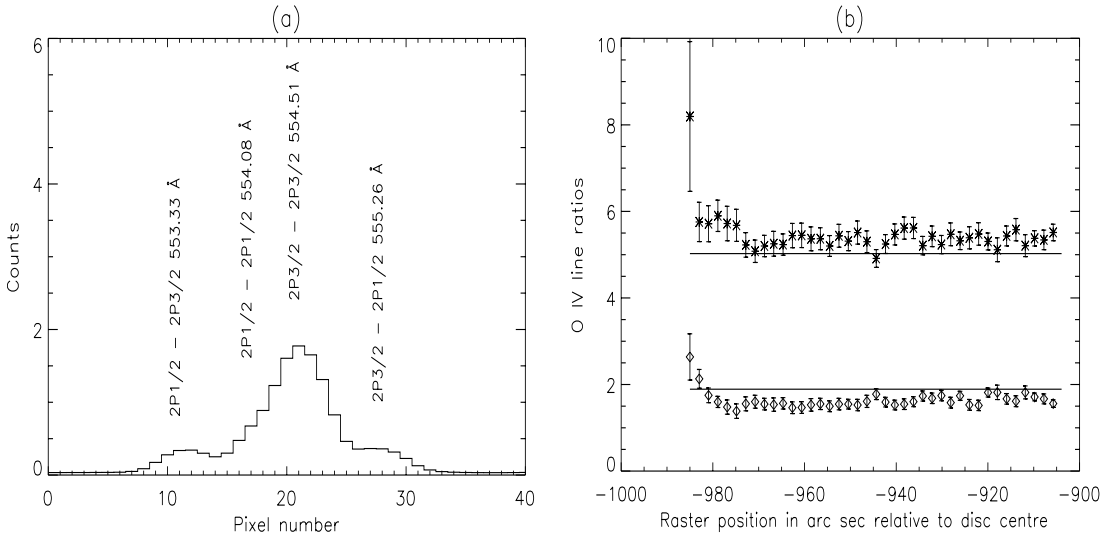

Fig. 9. a Spectral interval spanning the O IV $2s^2 2p\ ^2P$ - $2s2p^2\ ^2P$ multiplet at 554 Å. **b** Branching line intensity ratios vs. raster position over the East solar limb. The upper set of values corresponds to the I(3/2-3/2)/I(1/2-3/2) ratio and the lower set to the I(1/2-1/2)/I(3/2-1/2) ratio. The full line shows the corresponding A-value ratio.

3.2.1. O IV $2s^2 2p\ ^2P$ - $2s2p^2\ ^2S$ (608 Å)

The 3/2-1/2 component at 609.29 Å is severely blended with the stronger Mg X $2s\ ^2S_{1/2}$ - $2p\ ^2P_{3/2}$ (609.79 Å) line. In principle it should be possible to evaluate the O IV line intensity by subtracting the intensity of the Mg X line estimated from its density insensitive ratio to the other line ($2s\ ^2S_{1/2}$ - $2p\ ^2P_{1/2}$) of the Mg X doublet at 624.95 Å. This, however, would introduce further uncertainties to the O IV line intensity and so the data were not analysed.

3.2.2. O IV $2s^2 2p\ ^2P$ - $2s2p^2\ ^2P$ (554 Å)

This multiplet is well separated from other lines and no significant line blending is expected. The on-disk spectrum is shown in Fig. 9a. The fitting of the O IV multiplet was made slightly difficult by the 1/2-1/2 transition not being well resolved from the strongest line of the multiplet (3/2-3/2).

The intensity ratios I(3/2-3/2)/I(1/2-3/2) and I(1/2-1/2)/I(3/2-1/2) are plotted in Fig. 9b along with the corresponding A-value ratios. In both cases experiment and optically thin theory agree both on the disk and above the limb through the O IV layer. Well above the limb, there appears to be some deviation from the optically thin ratio but here the experimental data are more uncertain because of the weaker signals. There is some scatter of the experimental results on the disk. To see if there was any effect depending on the line intensity we divided the data along the slit into two equal cohorts comprising the average of pixels with the more intense and less intense emission. The data were then fitted and the same intensity ratios calculated. As shown in Fig. 10 there is essentially no difference between the two datasets themselves and the original intensity ratios plotted in Fig. 9b.

4. Escape probability analysis

Jordan (1967) introduced the simple idea of extracting optical depths from observations of intensity ratios of spectral lines arising from a common upper level. She wrote the ratio of the energy emissivities of lines 1 and 2 as

$$\frac{E_1}{E_2} = \frac{b_1 q_1}{\lambda_1} \frac{\lambda_2}{b_2 q_2} \tag{1}$$

where q_1 and q_2 are the escape probabilities, b_1 and b_2 the probabilities that photons will be emitted in lines 1 and 2 respectively and the λ's are the line wavelengths. Earlier, other authors had introduced ideas of escape probabilities for describing both emergent intensities (Holstein, 1947) and excited state population structures (McWhirter 1965) and since then escape probabilities and escape factors have been developed extensively by eg. Irons (1979) and more recently Kastner & Kastner (1990). Doyle & McWhirter (1980), using the same approach as Jordan, considered branching ratios to investigate opacity in spectral lines of C III at the limb of the sun utilising for this purpose Skylab cross-limb observations. They used a more sophisticated escape probability expression than Jordan which they called g, given by

$$g\{\tau_0\} = \frac{1}{\sqrt{\pi}} \int_{-\infty}^{\infty} e^{-x^2}\, exp\{-\tau_0 e^{-x^2}\}\, dx. \tag{2}$$

This is identical to what Irons (1979) called the transmission factor, $T(\tau_0)$, and what Kastner & Kastner (1990) termed $p_f(\hat{\nu}, \vec{k}, \tau : 0)$. $g\{\tau_0\}$ represents the probability that a photon emitted at an optical depth τ_0 in the direction of the line of sight will propagate along the line of sight without being absorbed. Kastner & Kastner describe this as the case of isolated emitters and absorbers (denoted by '0') as it does not include the effect of emission at other optical depths along the line of sight. Averaging this expression along the line of sight leads to what Kastner

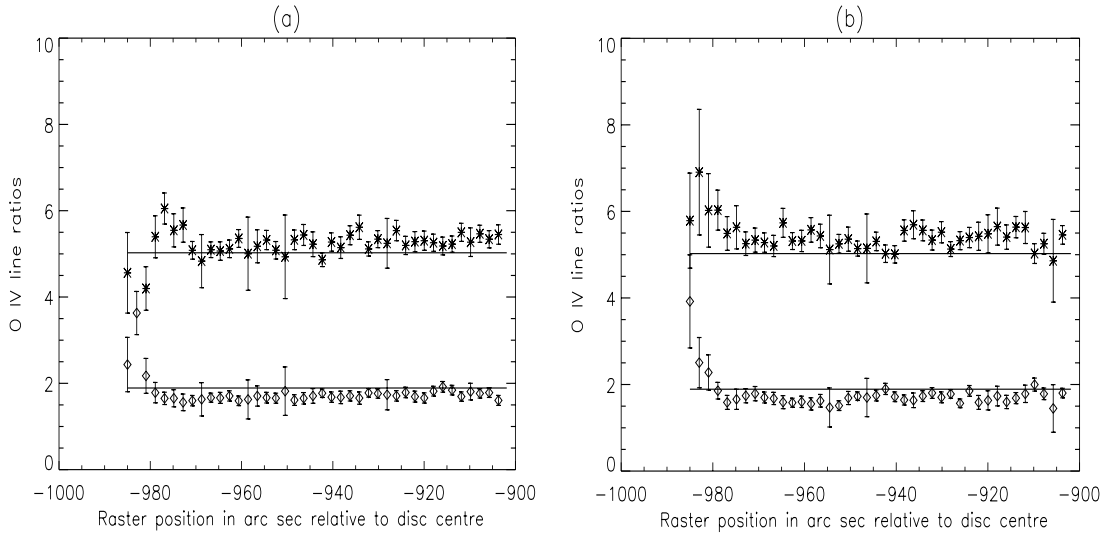

Fig. 10a and b. The same O IV intensity ratios as plotted in Fig. 9b divided into (**a**) the less intense pixels and (**b**) the more intense pixels averaged spectra.

& Kastner describe as being the proper escape probability for emergent intensities, given by

$$\bar{g}\{\tau_0\} \equiv p_f(\hat{\nu}, \vec{k}, \tau : 1) = \frac{1}{\sqrt{\pi}} \int_{-\infty}^{\infty} \left\{ \frac{1 - exp[-\tau_0 e^{-x^2}]}{\tau_0} \right\} dx. \quad (3)$$

This represents the *mean* probability that a photon emitted from some point in a layer of optical depth τ_0, in the direction of the line of sight, will escape along the line of sight.

The expression assumes that the only effect of opacity is to scatter photons out of the line of sight which is not true as photons may also be scattered into the line of sight. This was recognised by Jordan (1967) who wrote

$$E_i \sim N_u W_i = \frac{N_u b_i q_i}{1 - \sum_n (b_n[1 - q_n])} \quad (4)$$

where W_i is the fraction of photons created, escaping in line i; q_i is equivalent in principle to $\bar{g}\{\tau_0\}$ and the denominator accounts for the scattering into the line of sight. This was subsequently re-written by Kastner & Bhatia (1992) as the correct line of sight escape probability, p_e, where

$$p_{e,j} = \frac{\vec{p}_{f,j}}{1 - \sum_i b_i (1 - p_{d,i})(1 - \bar{p}_{f,i})(1 - \vec{p}_{f,i})} \quad (5)$$

where $p_{d,i}$ is the photon loss probability, $\vec{p}_{f,j} = p_f(\hat{\nu}, \vec{k}, \tau : 1) \equiv \bar{g}\{\tau_0\}$, and $\bar{p}_{f,i} = p_f(\hat{\nu}, \hat{\vec{k}}, \tau : 0)$. $\bar{p}_{f,i}$ is the mean probability that a photon emitted anywhere in the layer will travel to the surface and escape. This latter term is equivalent to Irons' escape factor, θ.

It was pointed out by Jordan, however, that for intensity ratios of lines arising from a common upper level the denominator of $p_{e,j}$ cancels out leaving just $\vec{p}_{f,j} \equiv \bar{g}\{\tau_0\}$ as the appropriate escape probability for this ratio analysis.

4.1. The escape probability

Since we are following the approach of Doyle & McWhirter it is instructive to consider the effects of using the less appropriate transmission factor, g (Eq. 2), compared with the escape probability $\bar{g}$ (Eq. 3). $\bar{g}$ may be obtained from g as follows: Following McWhirter (1965) the optical thickness of a spectral line at line centre is

$$\tau_0 = 1.16^{-6} \sqrt{M/T_i} \lambda_0 N_l f_{l \to u} L \quad (6)$$

where T_i is the ion temperature (K), M is the atomic mass number, λ_0 is the central wavelength (cm), N_l is the number density of the lower level of the transition (cm^{-3}), $f_{l \to u}$ is the absorption oscillator strength and L (cm) is the physical thickness of the plasma along the line of sight. We introduce the absorption coefficient κ_ν at the frequency ν in the dependence of the escape factor. Take the origin of coordinates at the outer intersection of the viewing line with the boundary of the emitting layer and $-x_2$ as the intersection of the viewing line with the inner boundary. Assume that emission and absorption profiles are identical ($= \phi(\nu)$) and that the Einstein B-coefficient is defined in terms of energy density. Then the equation of radiative transfer, integrated over frequency gives

$$\begin{aligned} \frac{d\bar{I}}{dx} &= (1/4\pi) A_{u \to l} N_u - (1/c) B_{l \to u} h\nu_0 N_l \int I_\nu \phi(\nu) d\nu \\ &= (1/4\pi) A_{u \to l} N_u \left[1 - \frac{N_l \omega_u}{N_u \omega_l} \frac{c^2}{2\nu_0^2} I \right] \\ &= (1/4\pi) A_{u \to l} N_u g\{\kappa_{0,l \to u} x\} \end{aligned} \quad (7)$$

where $\bar{I} = \int I_\nu d\nu$, $I = \int I_\nu \phi(\nu) d\nu$ and $g\{\kappa_{0,l \to u} x\}$ is the probability of escape from the point x in the plasma towards the line of sight. $\kappa_{0,l \to u}$ is the absorption coefficient at line centre. For a Doppler broadened line, introducing the absorption profile of the line with the central frequency of the spectral line as ν_0, corresponding to the central wavelength λ_0, we have the

following connections

$$\phi(\nu) = \frac{1}{\sqrt{\pi}\Delta\nu_D} exp\{-(\nu-\nu_0)^2/\Delta\nu_D^2\} \quad (8)$$

with

$$\int \phi(\nu)d\nu = 1,\ \Delta\nu_D = \alpha\nu_0\sqrt{\frac{M_p}{M}\frac{m_e}{M_p}\frac{kT_i}{I_H}}. \quad (9)$$

The absorption coefficient κ_ν, defined in terms of energy absorption per steradian is

$$\begin{aligned}\kappa_\nu &= N_l B_{l\to u}(\frac{h\nu}{c})\phi(\nu)\\ &= \pi\alpha^2 c a_0 N_l f_{l\to u}\phi(\nu)\\ &= \sqrt{\pi}\alpha a_0 N_l f_{l\to u}\sqrt{\frac{M}{M_p}\frac{M_p}{m_e}\frac{I_H}{kT_i}}(\frac{c}{\nu_0})\\ &\quad exp\{-(\nu-\nu_2)^2/\Delta\nu_D^2\}. \end{aligned} \quad (10)$$

Define also

$$\bar{\kappa} = N_l B_{l\to u}(\frac{h\nu_0}{c}) = \frac{\kappa_\nu}{\phi(\nu)} \quad (11)$$

and

$$\kappa_0 = N_l B_{l\to u}\frac{h\nu_0}{c}\frac{1}{\sqrt{\pi}\Delta\nu_D} = \frac{1}{\sqrt{\pi}\Delta\nu_D}\bar{\kappa}. \quad (12)$$

Returning to the intensity calculation, assume that the ion populations are independent of position in the layer and correspond to those from an optically thin collisional-radiative model. Then the observed intensity is

$$\begin{aligned}\bar{I} &= (1/4\pi)A_{u\to l}N_u\int_0^{x_2} g\{\kappa_{0,l\to u}x\}dx\\ &= (1/4\pi)A_{u\to l}N_u\int_0^{\Delta x} g\{\kappa_{0,l\to u}x\}dx \quad (13)\\ &= (1/4\pi)A_{u\to l}N_u\Delta x\bar{g}\{\kappa_{0,l\to u}\Delta x\} \quad (14)\end{aligned}$$

where $\bar{g}$ is the averaged escape factor over the layer and $\Delta x = x_2$ is the thickness of the layer.

$$g\{\kappa_0 x\} = \frac{1}{\sqrt{\pi}}\int_{-\infty}^{\infty}[exp\{-\kappa_0(x_2-x)e^{-u^2}\}]\,e^{-u^2}du. \quad (15)$$

Then

$$\bar{g}\{\kappa_0\Delta x\} = \frac{1}{\sqrt{\pi}}\int_{-\infty}^{\infty}\left[\frac{1-exp\{-\kappa_0\Delta x e^{-u^2}\}}{\kappa_0\Delta x}\right]du. \quad (16)$$

Reintroduce $\tau_0 = \kappa_0\Delta x$. For two lines with common upper level u and lower levels l_1 and l_2, the observed intensity ratio is

$$\frac{\bar{I}_{u\to l_1}}{\bar{I}_{u\to l_2}} = \frac{A_{u\to l_1}}{A_{u\to l_2}}\frac{\bar{g}\{\tau_{0,l_1\to u}\}}{\bar{g}\{\tau_{0,l_2\to u}\}} \quad (17)$$

From Eq. 6,

$$\tau_{0,l_1-u} = \tau_{0,l_2-u}\frac{N_{l_1}f_{l_1\to u}}{N_{l_2}f_{l_2\to u}}. \quad (18)$$

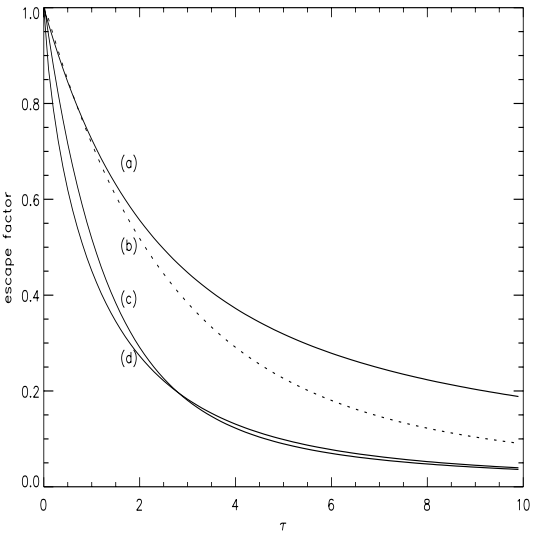

Fig. 11. Comparison of escape factors versus optical depth τ. (a) the layer averaged emergent flux escape factor $\bar{g}(\tau)$; (b) $g(\tau/2)$; (c) the emergent flux escape factor $g(\tau)$; (d) the population escape factor $\bar{\bar{g}}(\tau)$.

Provided the ratio of the two lower level population densities is not influenced by self absorption and can be estimated, then the optical depth of the lines may be inferred from the observed intensity ratio using Eq. 17. Doyle and McWhirter applied this analysis to pure branching ratios of the C III $2s2p\,^3P$ - $2p^2\,^3P$ (1175 Å) multiplet for which the lower 'metastable fine structure' levels have close to relative statistical populations at solar atmosphere densities.

To see how the use of g rather than $\bar{g}$ compares, recall Eq. 13 and use the intermediate value theorem so that

$$\bar{I} = (1/4\pi)A_{u\to l}N_u g\{\overline{\kappa_{0,l\to u}x}\}\Delta x \quad (19)$$

where $\overline{\kappa_{0,l\to u}x} \equiv \bar{\tau}_0$ is some value of τ_0 such that $0 \le \bar{\tau}_0 < \tau_0$. Thus the Doyle and McWhirter analysis seems to require that g replaces $\bar{g}$ and $\bar{\tau}_0$ replaces τ_0. However, the question arises as to whether Eq. 18 is valid with $\bar{\tau}_0$ replacing τ_0. We can write $\bar{\tau}_0 = \Delta(\tau_0)\tau_0$. For $\tau_0 < 1$ it can be seen from Fig. 11 that $\Delta \approx 1/2$ which is to say that the *mean* probability of escape from a layer of optical depth less than 1 is equivalent to the probability of escape from the centre of the layer. However, it can also be seen from Fig. 11 that for optical depths larger than 1, $\Delta < 1/2$ as expected since for layers of optical depth greater than 1 not all of the layer is 'seen'. The implication for the opacity deduction from this is that

$$\frac{\bar{\tau}_{0,l_1-u}}{\bar{\tau}_{0,l_2-u}} = \frac{\tau_{0,l_1-u}}{\tau_{0,l_2-u}}\frac{\Delta(\tau_{0,l_1-u})}{\Delta(\tau_{0,l_2-u})} \neq constant \quad (20)$$

and the use of g instead of $\bar{g}$ is inappropriate for optical depths greater than 1.

4.2. Opacity deduction from observed branching line ratios

Following the Doyle and McWhirter analysis, the relative optical depths of the two lines of the ratio are obtained from

Table 2. Summary of NIS and GIS B-like ion multiplets suitable for opacity analysis. Lines marked * are also detected by SUMER.

Multiplet	Spectrometer	Comments
N III $2s^2 2p\ ^2P$ - $2s2p^2\ ^2P$ (684 Å)	GIS-4*	blending
N III $2s^2 2p\ ^2P$ - $2s2p^2\ ^2S$ (763 Å)	GIS-4*	blending
O IV $2s^2 2p\ ^2P$ - $2s2p^2\ ^2P$ (554 Å)	NIS-2	suitable for analysis
O IV $2s^2 2p\ ^2P$ - $2s2p^2\ ^2S$ (608 Å)	NIS-2	severe blending
Ne VI $2s^2 2p\ ^2P$ - $2s2p^2\ ^2P$ (400 Å)	GIS-3	blending
Ne VI $2s^2 2p\ ^2P$ - $2s2p^2\ ^2S$ (434 Å)	GIS-3	blending

Table 3. Summary of the data for C III $2s2p\ ^3P_2 - 2p^2\ ^3P_2$ transition for each raster scan position. $\tau_{0,2-2}/\tau_{0,1-2} = 3.204$

Pos.(")	$\tau_{0,2-2}$	$\bar{g}_{2-2}$	$\bar{\tau}_{0,2-2}$	g_{2-2}	Pos.(")	$\tau_{0,2-2}$	$\bar{g}_{2-2}$	$\bar{\tau}_{0,2-2}$	g_{2-2}
943.06	0.74	0.78	0.35	0.80	959.94	-	-	4.29	0.11
944.94	0.93	0.74	0.43	0.75	961.88	8.07	0.22	1.97	0.30
946.81	1.08	0.71	0.49	0.72	963.75	1.65	0.61	0.71	0.63
948.69	1.26	0.67	0.56	0.69	965.63	1.25	0.68	0.56	0.69
950.56	1.04	0.72	0.47	0.73	967.50	1.40	0.65	0.62	0.66
952.44	1.16	0.69	0.52	0.71	969.38	1.78	0.59	0.76	0.61
954.31	1.83	0.58	0.77	0.60	971.25	1.64	0.61	0.71	0.63
956.19	3.34	0.42	1.22	0.45	973.13	2.20	0.53	0.90	0.55
958.06	-	-	3.05	0.18	975.00	2.09	0.55	0.86	0.57

Table 4. Summary of the data for C III $2s2p\ ^3P_0 - 2p^2\ ^3P_1$ transition for each raster scan position. $\tau_{0,0-1}/\tau_{0,2-1} = 0.779$. Since the opacity ratio is fairly close to unity, the absolute opacities inferred here are expected to have large errors and would be more reliably modelled from the 2-2 opacity of the previous table (see Sect. 4.4).

Pos.(")	$\tau_{0,0-1}$	$\bar{g}_{0-1}$	$\bar{\tau}_{0,0-1}$	g_{0-1}	Pos.(")	$\tau_{0,0-1}$	$\bar{g}_{0-1}$	$\bar{\tau}_{0,0-1}$	g_{0-1}
943.06	0.77	0.78	0.34	0.80	959.94	2.42	0.51	0.79	0.59
944.94	0.98	0.73	0.42	0.76	961.88	1.01	0.72	0.43	0.75
946.81	1.22	0.68	0.50	0.72	963.75	0.85	0.76	0.37	0.78
948.69	1.28	0.67	0.52	0.71	965.63	1.13	0.70	0.47	0.73
950.56	0.91	0.75	0.39	0.77	967.50	0.45	0.86	0.21	0.88
952.44	1.05	0.72	0.44	0.75	969.38	1.16	0.69	0.48	0.73
954.31	1.14	0.70	0.47	0.73	971.25	0.84	0.76	0.36	0.79
956.19	1.63	0.61	0.62	0.66	973.13	0.01	1.00	0.01	1.00
958.06	1.85	0.58	0.67	0.64	975.00	0.00	1.00	0.00	1.00

Eq. 17. The relative populations in the lower levels were examined in an optically thin population calculation (see Sect. 4.4) at $T_e = 8.0 \times 10^4 K$, $N_e = 5 \times 10^{10}$ cm^{-3} for C III and $T_e = 4.0 \times 10^4 K$, $N_e = 10^{11}$ cm^{-3} for C II. The electron temperatures, T_e, were taken from the peak of the $G(T_e)$ functions (at fixed pressure) for the lines and the electron density, N_e, from the Vernazza et al. (1981) model. For C III, the electron density from the model is significantly larger than that typically used for quiet sun ($N_e \sim 8 \times 10^9$ cm^{-3}). At the model density, the fine structure levels of the lower metastable term are closely relatively statistically populated (ratios 1:3:5). This is not so at the lower density when the decay via the $2s2p\ ^1P$ mixing reduces the $^3P_1$ relative population (ratios 1:2.8,5.0). If these fine structure population ratios were sensitive to opacity then it would violate the conditions for Eq. 18. We have investigated the effect of optical depth on these ratios using the ADAS code ADAS214 (see Sect. 5). The opacity modified ratios are 1:3.1:4.7 The self-absorption as expected drives the $^3P_1$ population closer to its statistical proportion. However the effect is weak and so, for the purposes of the present paper, little error is introduced by using the optically thin metastable fine structure population ratios. We have adopted the ratios at $N_e = 2 \times 10^{10}$ cm^{-3} as representative. For the C II case the lower ground term relative populations are very close to statistical, insensitive to the plasma conditions and unchanged at finite optical depths. Then in both cases Eq. 17 is used with the theoretical escape probabilities and experimental intensity ratios to deduce the optical depth in one of the lines in each ratio. Tables 3 to 7 summarise the values of τ_0, $\bar{g}$, $\bar{\tau}_0$ and g at different solar positions across the limb from the C III and C II multiplet branching ratios. An original objective was to choose multiplets for different members of the same isoelectronic sequences, for example C II, N III and O IV to show the progression of optical depth effects along sequences. The multiplets amenable to analysis provide only a direct comparison of C II and O IV which show a marked reduction of optical thickness along the sequence. Dissimilar multiplets in C

Table 5. Summary of the data for C II $2s^2 2p\ ^2P_{3/2} - 2s2p^2\ ^2S_{1/2}$ transition for each raster scan position. $\tau_{0,3/2-1/2}/\tau_{0,1/2-1/2} = 1.97$.

Pos.(")	$\tau_{0,3/2-1/2}$	$\bar{g}_{3/2-1/2}$	$\bar{\tau}_{0,3/2-1/2}$	$g_{3/2-1/2}$	Pos.(")	$\tau_{0,3/2-1/2}$	$\bar{g}_{3/2-1/2}$	$\bar{\tau}_{0,3/2-1/2}$	$g_{3/2-1/2}$
943.06	4.56	0.34	1.37	0.41	959.94	7.40	0.24	1.67	0.35
944.94	4.52	0.34	1.37	0.41	961.88	5.04	0.32	1.44	0.40
946.81	4.30	0.35	1.33	0.42	963.75	2.58	0.49	0.97	0.53
948.69	4.81	0.33	1.41	0.40	965.63	0.34	0.89	0.17	0.90
950.56	5.20	0.31	1.46	0.39	967.50	0.34	0.89	0.16	0.90
952.44	5.02	0.32	1.41	0.40	969.38	-	-	-	-
954.31	5.50	0.30	1.50	0.38	971.25	-	-	-	-
956.19	4.91	0.32	1.42	0.40	973.13	-	-	-	-
958.06	5.14	0.31	1.45	0.39	975.00	-	-	-	-

Table 6. Summary of the data for C II $2s^2 2p\ ^2P_{3/2} - 2s2p^2\ ^2P_{1/2}$ transition for each raster scan position. $\tau_{0,3/2-1/2}/\tau_{0,1/2-1/2} = 0.507$. The opacity ratio is again fairly close to unity and the comments on Table 5 apply.

Pos.(")	$\tau_{0,3/2-1/2}$	$\bar{g}_{3/2-1/2}$	$\bar{\tau}_{0,3/2-1/2}$	$g_{3/2-1/2}$	Pos.(")	$\tau_{0,3/2-1/2}$	$\bar{g}_{3/2-1/2}$	$\bar{\tau}_{0,3/2-1/2}$	$g_{3/2-1/2}$
943.06	0.66	0.80	0.29	0.83	959.94	0.33	0.89	0.15	0.91
944.94	0.47	0.85	0.21	0.87	961.88	0.39	0.87	0.18	0.89
946.81	0.31	0.90	0.14	0.91	963.75	0.12	0.96	0.06	0.97
948.69	0.12	0.96	0.06	0.97	965.63	0.14	0.95	0.07	0.97
950.56	0.33	0.89	0.15	0.91	967.50	0.10	0.97	-	-
952.44	0.49	0.85	0.22	0.87	969.38	1.50	0.63	0.54	0.70
954.31	0.47	0.85	0.21	0.87	971.25	1.47	0.64	0.53	0.70
956.19	0.19	0.94	0.09	0.95	973.13	8.46	0.21	0.99	0.52
958.06	0.43	0.86	0.20	0.88	975.00	-	-	1.41	0.40

Table 7. Summary of the data for C II $2s^2 2p\ ^2P_{3/2} - 2s2p^2\ ^2P_{3/2}$ transition for each raster scan position. $\tau_{0,3/2-3/2}/\tau_{0,1/2-3/2} = 5.05$.

Pos.(")	$\tau_{0,3/2-3/2}$	$\bar{g}_{3/2-3/2}$	$\bar{\tau}_{0,3/2-3/2}$	$g_{3/2-3/2}$	Pos.(")	$\tau_{0,3/2-3/2}$	$\bar{g}_{3/2-3/2}$	$\bar{\tau}_{0,3/2-3/2}$	$g_{3/2-3/2}$
943.06	4.95	0.32	1.64	0.36	959.94	4.69	0.33	1.58	0.37
944.94	5.01	0.32	1.65	0.35	961.88	4.84	0.33	1.61	0.36
946.81	4.13	0.36	1.46	0.39	963.75	4.40	0.35	1.52	0.38
948.69	4.37	0.35	1.51	0.38	965.63	2.88	0.46	1.13	0.48
950.56	5.15	0.31	1.68	0.35	967.50	2.36	0.51	0.96	0.53
952.44	4.81	0.33	1.61	0.36	969.38	1.07	0.71	0.49	0.72
954.31	4.56	0.34	1.55	0.37	971.25	1.40	0.65	0.62	0.66
956.19	5.23	0.31	1.69	0.34	973.13	1.63	0.61	0.71	0.62
958.06	5.10	0.31	1.67	0.35	975.00	1.29	0.67	0.58	0.68

II and C III again indicate a strong reduction of optical thickness with increasing ion charge. The results available here suggest that neutral to doubly ionised ions are the principal concerns for optical depth effects on differential emission measure analysis.

4.3. Modelling opacity variation in branching ratios at the limb

For a spherically symmetric stratified atmosphere, the extension of the geometrical length of an emitting layer along the line of sight at longitudes approaching the limb from the disk is the determinate factor in optical thickness variation. For thin emitting layers therefore, the variation of optical depths and branching ratios are also geometrically determined (Doyle & McWhirter 1980). We propose a simple two layer model. Assume that the layer may be divided into two parts, namely a potentially optically thick primary layer where the ionisation stage has its peak abundance (called the 'inner model') and an optically thinning outer layer where the population densities are rapidly decreasing (called the 'outer model'). The peak emission of an emitting layer is in the line of sight for all raster positions across the disk up to the radial location of the emitting layer at the limb. In Fig. 12, the theoretical curve for C III of $A_{2-2}\bar{g}\{\tau_{0,2-2}^{(theor)}\}/A_{1-2}\bar{g}\{\tau_{0,1-2}^{(theor)}\}$ versus position relative to disc centre has been superimposed on the experimental intensity ratio data. Here $\tau_0^{(theor)} = \tau_0^c\ \delta/cos\theta$ with $\delta = 1$ inside the visible limb and $\delta = 2$ outside the visible limb. τ_0^c is the optical depth at disc centre. Note that the approximation of variation as $cos\theta$ (cf. Doyle and McWhirter) breaks down at angles near $\pi/2$ depending on emitting layer thickness. The position (in arc sec relative to the disc centre) of the C III layer and τ_0^c are treated

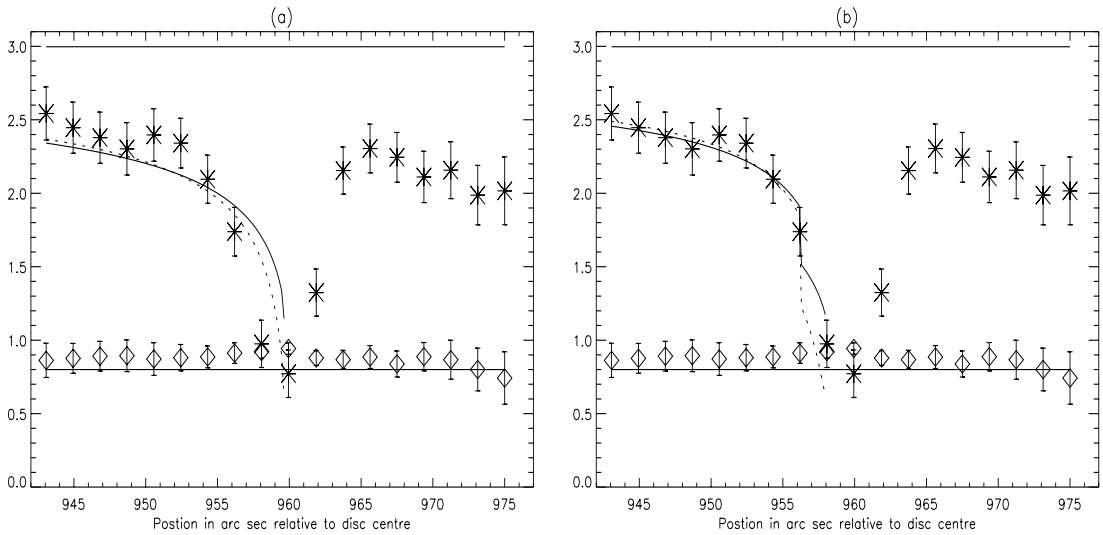

Fig. 12. **a** Calculated intensity ratios for the C III $2s2p\ ^3P$ - $2p^2\ ^3P$ (1175 Å) multiplet component ratios I(2-2)/I(1-2) and I(0-1)/I(2-1) vs raster position in arc sec relative to the disc centre compared with the observed ratios. The calculated results use the position for the visible limb from the telemetry (959.60 arc sec) The solid curve uses $\bar{g}$ and the dashed line, g in the calculation. **b** The same multiplet component ratios are shown, but the position of the visible limb is shifted to optimise the match between theory and experiment. The shifted limb position is at 956.20 arc sec.

as variables chosen to minimise the functional

$$\sum_{i=1}^{9}[A_{2-2}\ \bar{g}\{\tau_{0,2-2}^{(theor)}\}/A_{1-2}\ \bar{g}\{\tau_{0,1-2}^{(theor)}\} - I_{2-2}/I_{1-2}]^2 \quad (21)$$

Fig. 12a uses the nominal angular position of the visible limb from the observing sequence telemetry. Positional error in SUMER is ~ 10 arc sec. We have therefore conducted a further fit, shown in Fig. 12b, in which the visible limb position was varied to optimise the match of theory and observation. The optimised position is well within acceptable limits. Note also that the theoretical inner model curve based on our preferred $\bar{g}$ shows a significant improvement of fit compared with that using the Doyle and McWhirter g. We take this as support of the use of $\bar{g}$ in basic escape factor analysis.

For the region beyond the limb we consider three models. Firstly we consider an emitting atmosphere as predicted by the model of Vernazza et al. (1981) (henceforth referred to as the VAL model) which assumes that the temperature and density gradients in the transition region are determined by a constant conductive flux from the corona to the chromosphere. From this model we have $N_e(h)$ and $T_e(h)$ which we use in conjunction with the contribution function, $G(T_e)$, for a line with the assumption that

$$N_l \sim N_e(h)\bar{G}_{u\rightarrow l}(h) \quad (22)$$

where $\bar{G}_{u\rightarrow l}(h) \equiv G_{u\rightarrow l}(T_e(h))$. Thus the optical depth of a line is given by

$$\tau(h) = a\int_{l.o.s.} N_e(h)\bar{G}_{u\rightarrow l}(h)ds \quad (23)$$

where l.o.s. stands for *line of sight* and ds is an element of distance along the line of sight. Here a is a constant which is found by matching the inner and outer models at the layer edge. Fig. 13 shows the inner and outer models superposed on the experimental data for the C II $2s^2 2p\ ^2P$ - $2s2p^2\ ^2S$ (1036 Å) multiplet component ratio I(3/2-1/2)/I(1/2-1/2) and the C III $2s2p\ ^3P$ - $2p^2\ ^3P$ (1175 Å) multiplet component ratio I(2-2)/I(1-2). The inner and outer models give slightly different positions for the C III layer.

It is clear that in both cases the VAL model fails to describe the emission above the limb. The $G_{u\rightarrow l}(T_e)$ functions are sharply peaked in temperature and for C II and C III the peaks occur at temperatures corresponding to the very sharp decrease in temperature and density predicted by the hydrostatic atmosphere model. Consequently the predicted ratios move sharply to the optically thin value on reaching the layer edge.

It has been known for some time that the off-limb EUV emission is dominated, over the height range of interest here, by spicule-like structures. Several authors (eg. Mariska & Withbroe 1975; Mariska et al. 1978) have shown that models such as the VAL model are unable to predict the observed line intensities in this region and so it is no surprise that they also fail to predict the observed opacities.

Though the signal is dominated by inhomogeneities, our models are stratified as regards emergent intensitities and plane parallel as regards escape probabilities and so we envisage two alternative empirical models in an attempt to account for the spicular component to the observed signals. Firstly the notion of a spherical shell of constant density, as previously envisaged on-disk, was extended to beyond the limb. This follows the approach of Kastner & Bhatia (1992) who used such a model to capture the grosser characteristics of the spicular contribution to the signal. Consequently the chosen layer thickness was 5 arc sec.

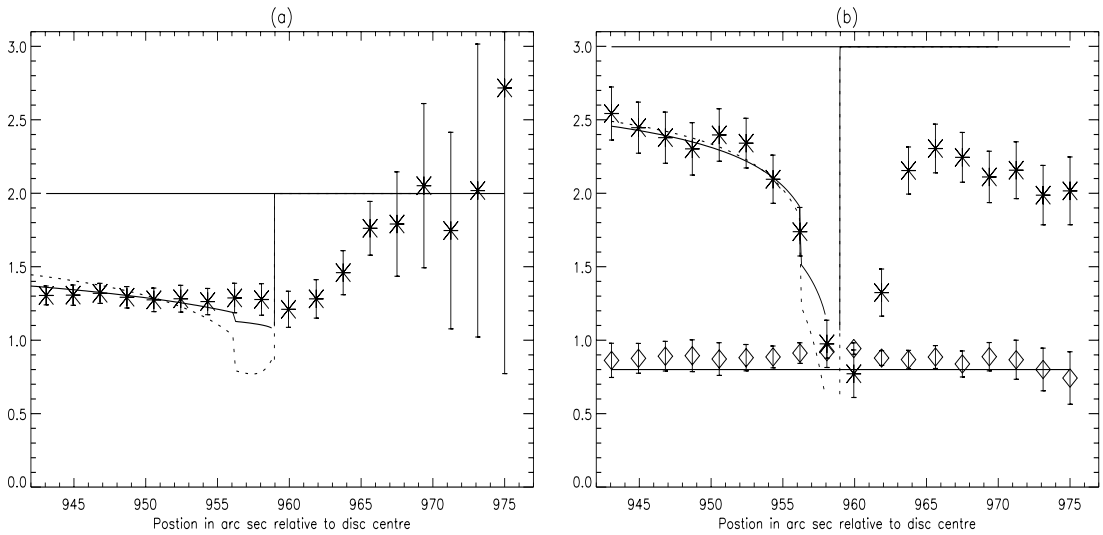

Fig. 13. **a** Calculated intensity ratio for the C II $2s^2 2p\ ^2P$ - $2s2p^2\ ^2S$ (1036 Å) multiplet component ratio I(3/2-1/2)/I(1/2-1/2) based on the VAL model vs raster position in arc sec relative to the disc centre compared with the observed ratios. The solid curve uses $\bar{g}$ and the dashed line, g. The shifted limb position at 956.20 arc sec is used. **b** Calculated intensity ratios for the C III $2s2p\ ^3P$ - $2p^2\ ^3P$ (1175 Å) multiplet component ratios I(2-2)/I(1-2) and I(0-1)/I(2-1) vs raster position in arc sec relative to the disc centre compared with the observed ratios.

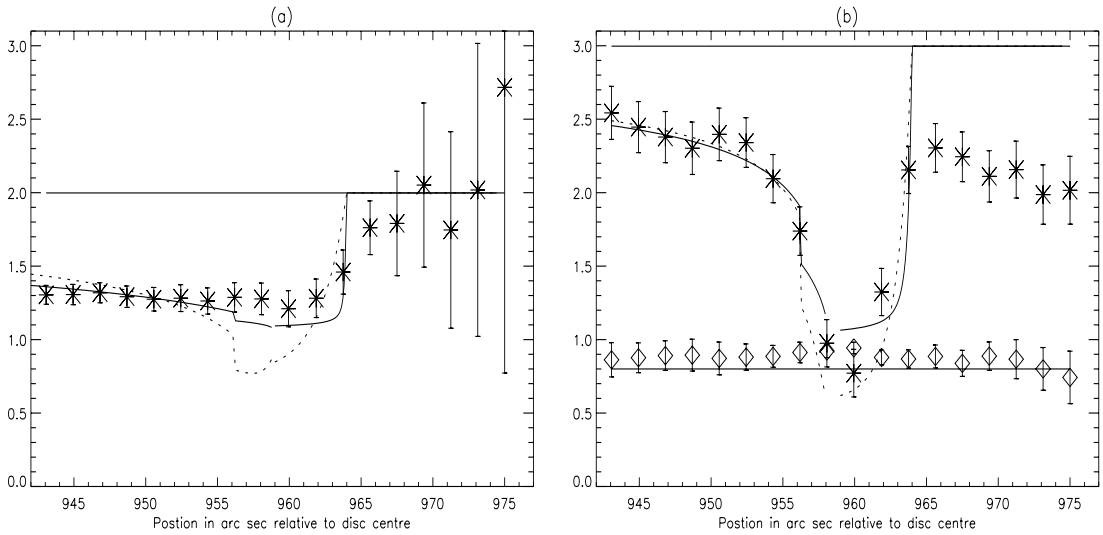

Fig. 14. **a** Calculated intensity ratio for the C II $2s^2 2p\ ^2P$ - $2s2p^2\ ^2S$ (1036 Å) multiplet component ratio I(3/2-1/2)/I(1/2-1/2) for a spherical shell of constant density vs raster position in arc sec relative to the disc centre compared with the observed ratios. The solid curve uses $\bar{g}$ and the dashed line, g. The shifted limb position at 956.20 arc sec is used. **b** Calculated intensity ratios for the C III $2s2p\ ^3P$ - $2p^2\ ^3P$ (1175 Å) multiplet component ratios I(2-2)/I(1-2) and I(0-1)/I(2-1) vs raster position in arc sec relative to the disc centre compared with the observed ratios.

Mariska, Feldman & Doschek considered models where the dominant contribution to the EUV signal was due to transition-zone sheaths around isolated cylindrical H_α spicules. They noted that 'above the emission peak the amount of emitting material in the line of sight for any spectral line must decrease exponentially with height with a scale height that depends on temperature'. In particular, they found that the density scale heights were around 1500km but decreased with decreasing electron temperature of line formation. Thus in our second empirical model we envisage a stratified emitting layer with a density variation versus height given by

$$N_l(h) = Bexp\left\{-\left(\frac{h-h_0}{H}\right)\right\} \tag{24}$$

where B is a constant, h_0 is the inner edge of the layer which is taken from the VAL model and H is the density scale height. These models are shown in Figs. 14 and 15 and they both represent a marked improvement on the VAL case with the exponential atmophere clearly the most effective. Upon optimising H in the latter model we get, when using $\bar{g}$, scale heights of 1.3 arc sec and 1.4 arc sec,equivalent to 942 km and 1015 km,

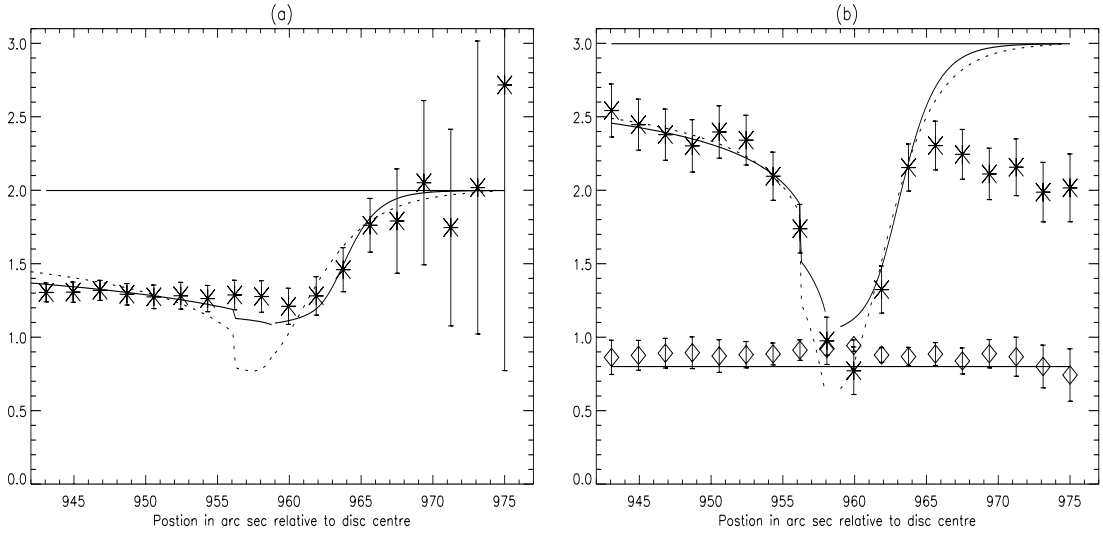

Fig. 15. a Calculated intensity ratio for the C II $2s^2 2p\,^2P$ - $2s2p^2\,^2S$ (1036 Å) multiplet component ratio I(3/2-1/2)/I(1/2-1/2) for the exponential atmosphere model vs raster position in arc sec relative to the disc centre compared with the observed ratios. The solid curve uses $\bar{g}$ and the dashed line, g. The shifted limb position at 956.20 arc sec is used. **b** Calculated intensity ratios for the C III $2s2p\,^3P$ - $2p^2\,^3P$ (1175 Å) multiplet component ratios I(2-2)/I(1-2) and I(0-1)/I(2-1) vs raster position in arc sec relative to the disc centre compared with the observed ratios.

for the C II and C III cases respectively. These are smaller than that suggested by Mariska, Feldman & Doschek but do decrease with decreasing temperature of line formation.

A feature of all three models considered is that the ratios all return to the optically thin limit whereas in the C III case the observed ratios do not. Referring to Fig. 6 it is clear to see that at large heights, beyond 965 arc sec say, the observed fluxes are very weak which is suggestive of low opacity yet the ratios indicate opacities at these heights similar to those on disk. It is our feeling, as suggested in Sect. 2.4, that the signal at these heights is dominated by instrumentally scattered light which comprises of light from the whole disk and so it is expected that such a signal would reflect similar opacities to those on disk. As discussed in Sect. 2.5, the C II ratios are ambiguous in this region and so no conclusions may be drawn about the success, or otherwise, of the models here.

4.4. Population modelling for optically thin to moderately optically thick plasma

We can compare ratios of intensities of component lines of a multiplet which do not have the same upper level. However, in this case N_u does not cancel in the ratio although the physical layer thickness Δx does. Thus the replacement of Eq. 17 for the intensity ratio is

$$\frac{\bar{I}_{u_1\to l_1}}{\bar{I}_{u_2\to l_2}} = \frac{A_{u_1\to l_1}}{A_{u_2\to l_2}} \frac{\bar{g}\{\tau_{0,l_1\to u_1}\}}{\bar{g}\{\tau_{0,l_2\to u_2}\}} \left(\frac{N_{u_1}}{N_{u_2}}\right)_\tau . \tag{25}$$

The suffix τ on the upper level population density ratio indicates that it depends in general on self absorption. Consider now the determination of the local population structure in a layer which is optically thick in the direction normal to the layer. We assume that the populations are independent of position in the layer and may be represented by the populations at the layer centre; also that the layer may be treated as plane parallel from the point of view of evaluating the radiation field at the centre of the layer. Take the origin of coordinates at the centre of the layer and let the layer have thickness $\Delta x = 2x_1$. For simplicity write the equation of radiative transfer as

$$\frac{dI_\nu}{dl} = j_\nu - \kappa_\nu I_\nu . \tag{26}$$

Evaluating the average over solid angle of the radiation intensity at the origin integrated over the layer

$$\begin{aligned}
\mathcal{I}_\nu(\mathbf{0}) &= \frac{2}{4\pi}\int_0^\pi 2\int_0^{x_1}\int_x^\infty \frac{j_\nu exp(-\kappa_\nu l)}{l^2} l\,dl\,dx\,d\theta \\
&= j_\nu\left[\int_{x_1}^\infty\int_0^{x_1}\frac{exp(-\kappa_\nu l)}{l}dx\,dl \right. \\
&\qquad \left. + \int_0^{x_1}\int_0^{l}\frac{exp(-\kappa_\nu l)}{l}dx\,dl\right] \\
&= j_\nu\left[\int_{x_1}^\infty \frac{x_1}{l}exp(-\kappa_\nu l)dl + \int_0^{x_1} exp(-\kappa_\nu l)dl\right] \\
&= \frac{j_\nu}{\kappa_\nu}\left[1 - exp(-\kappa_\nu x_1) + \kappa_\nu x_1 E_1(\kappa_\nu x_1)\right] .
\end{aligned} \tag{27}$$

Substituting $j_\nu = (1/4\pi)A_{u\to l}\phi(\nu)N_u$ and $\kappa_\nu = N_l B_{l\to u}(h\nu/c)\phi(\nu)$ into the local population equations, we have

$$\begin{aligned}
&\frac{dN_u}{dl} \\
&\quad = -A_{u\to l}N_u + N_l\int_{-\infty}^\infty (4\pi/c)B_{l\to u}\mathcal{I}_\nu\phi(\nu)\mathrm{d}\nu + ... \\
&\quad = -A_{u\to l}N_u\left[1 - \frac{N_l\omega_u}{N_u\omega_l}\int_{-\infty}^\infty (c^2/2\nu^2)\mathcal{I}_\nu\phi(\nu)\mathrm{d}\nu\right] + ...
\end{aligned}$$

$$= -A_{u\to l}N_u\left[1-\int_{-\infty}^{\infty}(\kappa_\nu/j_\nu)\mathcal{I}_\nu\phi(\nu)\mathrm{d}\nu\right]+...$$
$$= -A_{u\to l}N_u\bar{\bar{g}}\{\kappa_{0,l\to u}\Delta x\}+...\,. \quad (28)$$

Thus

$$\bar{\bar{g}}\{\kappa_{0,l\to u}\Delta x\}$$
$$= 1-(1/\sqrt{\pi})\int_{-\infty}^{\infty}[exp(\kappa_0\Delta x e^{-u^2}/2) + (\kappa_0\Delta x e^{-u^2}/2)E_1(\kappa_0\Delta x e^{-u^2}/2)]e^{-u^2}du \quad (29)$$

where we call $\bar{\bar{g}}$ the 'population escape factor'. It represents 1-the probability that a re-absorption event will occur at layer centre. Thus $\bar{\bar{g}}$ is equivalent to what Irons (1979) calls the 'Biberman-Holstein coefficient' evaluated at layer centre. We regard, however, $\bar{\bar{g}}$ as representing re-absorption characteristics of the emission layer as a whole so in this respect $\bar{\bar{g}}$ is equivalent to Irons' escape factor, θ. The graph of $\bar{\bar{g}}$ is also shown in Fig. 11. Provided the optical depth $\tau_{0,l\to u}=\kappa_{0,l\to u}\Delta x$ can be determined in one line then the optical depths and population escape factors of all other lines of the same ion connected to the same lower level may be calculated. For the ground term of ions of interest here, the levels are close to statistical relative populations in the optically thin plasma, thus the population escape factors of all lines connected to levels of the ground term may be determined. In the moderately thick case, we must also be concerned with lines connected to levels of the metastable term. It is a good approximation for ions relevant here that the metastable level populations are close to relative statistical populations and that the metastable term population remains close to its optically thin value relative to the ground term population (see the discussion in Sect. 4.2). Thus the population escape factors may be established for all relevant lines.

4.5. Classification of emergent spectral fluxes

We classify observed spectrum lines into five categories according to the influence of optical depth along the line of sight and of the influence of self absorption on the formation of the excited populations in the emitting layer. *Thin lines* (t) are those which are optically thin on the limb and whose emitting excited populations are not influenced (directly or indirectly) by self-absorption. *Modified thin lines* (mt) are optically thin on limb but their emitting populations are modified by the indirect effect of self absorption in other lines. *Weakly thin lines* (wt) are thin on the disk but thick on the limb, with their emitting populations unaffected by self absorption in other lines. *Modified weakly thin lines* (mwt) are optically thin on disk but their emitting populations are affected by self absorption in other lines and they are thick on limb. *Modified lines* (m) are lines whose emitting excited populations are influenced directly by self-absorption. We choose a 10% modification to the Einstein A coefficient as the criterion for assessing whether opacity affects either the emergent flux or the population structure. Indirect effects on populations are indicated by shifts at the 10% level at disk centre. Since $\bar{g}<0.9$ for $\tau_0>0.307$ and $\bar{\bar{g}}<0.9$ for $\tau_0>0.072$ the classification gives (i) *thin* $\Rightarrow\ \tau_0<0.307$ at the limb, populations unmodified; (ii) *modified thin* $\Rightarrow\ \tau_0<0.307$ at the limb, populations indirectly modified; (iii) *weakly thin* $\Rightarrow\ \tau_0<0.072$ on disk, $\tau_0>0.307$ at the limb, populations unmodified; (iv) *modified weakly thin* $\Rightarrow\ \tau_0<0.072$ on disk, $\tau_0>0.307$ at the limb, populations indirectly modified; (v) *modified* $\Rightarrow\ \tau_0>0.072$ on disk. Final disk centre results and line classifications are illustrated for C III and C II in Tables 8 and 9.

5. Computational implementation

The primary calculations were carried out within the framework of codes and data organisation of the Atomic Data and Analysis Structure, ADAS (Summers 1993,1999). Thus the spectral fitting used the code ADAS602 described earlier. Within ADAS, basic calculation of the populations of excited states of an ion in a plasma uses the code ADAS205. The code requires as input a structured dataset of ADAS data format adf04. Such data sets contain all the energy level, Einstein coefficients and collisional rate coefficients needed for the population calculation. The adf04 datasets used in this work were modified to include the population escape factors. ADAS205 was then executed in the usual manner. We have developed an ADAS procedure, ADAS214, to alter an adf04 dataset with the appropriate population escape factors based on a code by Behringer (1997). This new ADAS code includes simple plasma geometry models relevant to laboratory and astrophysical plasmas and will be described in a separate work. $G(T_e)$ contribution functions were also drawn from the ADAS database (adf20). These data are used in differential emission measure analysis and are described in Lanzafame et al. (1999).

6. Conclusions

The OPAC and ATRIC31 observing sequences conducted with SUMER and CDS have provided comprehensive, high quality rastered spectral data for opacity studies. In the present analysis, we have explored solar opacity for the low ionisation stages of first period elements motivated by the need for critical assessment of lines in differential emission measure analysis. The experimental data sets include spectra of second period ions which have been the subject of study previously in the solar chromosphere such as Si III (Keenan & Kingston 1986) and Si II (Lanzafame 1994). The latter was a detailed radiative transfer study. It is planned to revisit these ions in the solar atmosphere with the new data.

In our analysis of branching ratios, we have followed the escape probability method of Doyle and McWhirter. However, this simple escape probability approach is made more consistent if an appropriate layer averaged (or homogenous) escape probability is used. The improved comparison with the experimental data justifies this modification.

In the use of the geometrical variation of path length in cross-limb scans as a modelling check on the line ratio deductions, we have been able to extend the Doyle and McWhirter model to heights in the solar atmosphere above the height of peak emission. This is a consequence of the improved spectral signal

Table 8. Characterisation and classification of some spectrum lines of C III at disk centre.

Line	λ(Å)	f	τ_0	$\bar{\bar{g}}(\tau_0)$	$\bar{g}(\tau_0)$	Class
$2s2p\,^3P - 2p^2\,^3P$						
2-2	1175.711	0.221	0.156	0.836	0.947	m
1-1	1175.590	0.0713	0.0286	0.9521	0.990	mwt
2-1	1176.370	0.0715	0.0505	0.925	0.983	mwt
1-0	1175.987	0.0913	0.0366	0.942	0.987	wt
1-2	1174.933	0.1176	0.0471	0.929	0.984	mwt
0-1	1175.263	0.2792	0.0393	0.938	0.987	mwt
$2s2p\,^3P - 2s3s\,^3S$						
2-1	538.312	0.031	0.0100	0.979	0.997	wt
1-1	538.149	0.031	0.00569	0.987	0.998	t
0-1	538.075	0.031	0.00200	0.995	1.000	t
$2s2p\,^3P - 2s3d\,^3D$						
2-3	459.627	0.434	0.120	0.862	0.959	m
1-2	459.514	0.394	0.0617	0.914	0.979	wt
0-1	459.466	0.525	0.0289	0.951	0.990	wt
2-2	459.633	0.063	0.0174	0.968	0.994	wt
1-1	459.516	0.100	0.0157	0.970	0.995	wt
2-1	459.635	0.0042	0.00116	0.997	1.000	wt
$2s^2\,^1S - 2s2p\,^1P$						
0-1	977.020	0.746	0.665	0.628	0.802	m
$2s^2\,^1S - 2s3p\,^1P$						
0-1	386.203	0.220	0.0775	0.898	0.973	m
$2s^2\,^1S - 2s4p\,^1P$						
0-1	310.170	0.016	0.00453	0.989	0.999	t

Table 9. Characterisation and classification of some spectrum lines of C II at disk centre. The extrapolation to disk centre is subject to significant error in this case because of the relatively flat slope of the intensity ratio curve evident in Fig. 13a. A more secure classification would use direct measurements at the disk centre.

Line	λ(Å)	f	τ_0	$\bar{\bar{g}}(\tau_0)$	$\bar{g}(\tau_0)$	Class
$2s^22p\,^2P - 2s2p^2\,^2D$						
3/2-5/2	1335.709	0.115	0.628	0.638	0.812	m
1/2-3/2	1334.524	0.128	0.353	0.732	0.887	m
3/2-3/2	1335.665	0.027	0.147	0.842	0.950	m
$2s^22p\,^2P - 2s2p^2\,^2S$						
3/2-1/2	1037.012	0.129	0.643	0.634	0.808	m
1/2-1/2	1036.332	0.131	0.330	0.742	0.893	m
$2s^22p\,^2P - 2s2p^2\,^2P$						
3/2-3/2	904.143	0.405	1.760	0.433	0.590	m
1/2-1/2	903.958	0.331	0.727	0.611	0.787	m
3/2-1/2	904.481	0.0798	0.347	0.734	0.888	m
1/2-3/2	903.620	0.163	0.358	0.730	0.885	m
$2s^22p\,^2P - 2s^23s\,^2S$						
3/2-1/2	858.560	0.00615	0.0254	0.956	0.991	mwt
1/2-1/2	858.089	0.00404	0.00843	0.982	0.997	t
$2s^22p\,^2P - 2s^23d\,^2D$						
3/2-5/2	687.346	0.282	0.932	0.565	0.740	m
1/2-3/2	687.051	0.270	0.451	0.694	0.859	m
3/2-3/2	687.353	0.025	0.0826	0.893	0.972	m

quality of the new data. Of the three outer models considered, that of a stratified atmosphere with a density which falls off exponentially with height was the most successful, though none of the models include the effects of instrumentally scattered light which appears to dominate at large heights.

We have considered multiplet line ratios which are optically thick on disk as well as thick on limb for which the effect of self absorption on local excited population structure matters. Thus we have used a population escape factor, analogous to what Irons calls the Biberman-Holstein coefficient, to quantify this effect.

From these considerations, we have proposed a more comprehensive classification of opacity affected spectral lines and have been able to classify all the lines of an ion from observation of one of its multiplets.

In paper II of this series we extend the models considered here by using more sophisticated escape probabilities which include the modifications to the population structure, the effects of atmosphere inhomogeneities and the influence of scattered light.

Acknowledgements. GF acknowledges an EPSRC studentship and SL acknowledges an EPSRC-CASE studentship with the Rutherford Appleton Laboratory. SOHO is a project of international co-operation between ESA and NASA.

References

Behringer K.H., 1997, Max-Planck-Institut-fuer-Plasmaphysik report IPP 10/5
Brooks D.H., Fischbacher G.A., Fludra A., et al., 1999, A&A 347, 277
Curdt W., Feldman U., Laming J.M., et al., 1997, A&AS 126, 281
Doschek G.A., Vanhoosier M.E., Bartoe J.-D.F., et al., 1976, ApJS 31, 417
Doyle J.G., McWhirter R.W.P., 1980, MNRAS 193, 947
Harrison R.A., Sawyer E.C., Carter M.K., et al., 1995, Solar Physics 162, 233
Holstein T., 1947, Phys. Rev. 72, 1212
Irons, F.E., 1979, J. Quant. Spectrosc. Rad. Trans. 22, 1
Jordan C., 1967, Solar Physics 2, 441
Kastner S.O., Bhatia A.K., 1989, ApJS 71, 665
Kastner S.O., Bhatia A.K., 1992, ApJ 401, 416
Kastner S.O., Kastner R.E., 1990, J. Quant. Spectrosc. Rad. Trans. 44, No. 2, 275
Keenan F.P., Kingston A.E., 1986, MNRAS 220, 493
Lanzafame A.C., 1994, A&A 287, 972
Lanzafame A.C., Brooks D.H., Lang J., Summers H.P., Thompson A., 1999, A&A submitted
Mariska J.T., Feldman U., Doschek G.A., 1978, ApJ 226, 698
Mariska J.T., Withbroe G.L., 1975, Solar Physics 44, 55
McWhirter R.W.P., 1965, In: Huddlestone R.H., Leonard D.H. (eds.) Plasma Diagnostic Techniques. Academic Press
Summers H.P., 1993, JET Joint Undertaking Report. JET-IR(93)07
Summers H.P., 1999, The ADAS User Manual. version 2.1, http://patiala.phys.strath.ac.uk/adas/
Wilhelm K., Curdt W., Marsch E., et 1995, Solar Physics 162, 189
Withbroe G.L., Mariska J.T., 1976, Solar Physics 48, 21
Vernazza J.E., Avrett E.H., Loeser R., 1981, ApJS 45, 635